Journal of Alloys and Compounds 949 (2023) 169871

Contents lists available at ScienceDirect

Journal of Alloys and Compounds

journal homepage: www.elsevier.com/locate/jalcom

Influence of cooling rate on the microstructure and room temperature mechanical properties in the refractory $AlMo_{0.5}NbTa_{0.5}TiZr$ superalloy

Patricia Suárez Ocaño [a,*], Anna Manzoni [a], Inmaculada Lopez-Galilea [b], Benjamin Ruttert [b], Guillaume Laplanche [b], Leonardo Agudo Jácome [a]

[a] Bundesanstalt für Materialforschung und -prüfung (BAM), Department for Materials Engineering, Unter den Eichen 87, 12205 Berlin, Germany
[b] Institute for Materials, Ruhr-University Bochum, Universitätsstr. 150, 44801 Bochum, Germany

ARTICLE INFO

Article history:
Received 19 January 2023
Received in revised form 25 March 2023
Accepted 28 March 2023
Available online 29 March 2023

Keywords:
High entropy alloys
Mechanical properties
Fracture toughness
Microstructure
Nanoindentation

ABSTRACT

Refractory chemically complex alloys with bcc-based microstructures show great potential for high-temperature applications but most of them exhibit limited room-temperature ductility, which remains a challenge. One such example is the $AlMo_{0.5}NbTa_{0.5}TiZr$ alloy, mainly consisting of a nano-scaled structure with an ordered B2 matrix and a high-volume fraction of aligned cuboidal and coherently embedded A2 precipitates. This work aims to investigate how the cooling rate after hot isostatic pressing of the $AlMo_{0.5}NbTa_{0.5}TiZr$ alloy affects its microstructure and its resulting hardness and fracture toughness at room temperature. A slow cooling rate of 5 °C/min leads to a coarse microstructure consisting of aligned slabs (mean A2 precipitate ≈ 25 nm) with a nanohardness of about 8 GPa. In contrast, after the fastest cooling rate (30 °C/min), the A2 precipitates become more cubic with an edge length of ≈ 16 nm, resulting in an increase in nanohardness by 10 %. The fracture toughness is roughly independent of the cooling rate and its mean value (≈ 4.2 MPa·$m^{1/2}$) resembles that of some B2 intermetallics and other A2/B2 alloys. As the lattice misfit between the A2 and B2 phases is known to play a key role in microstructure formation and evolution, its temperature dependence between 20 and 900 °C was investigated. These findings offer insights into the evolution of the microstructure and room-temperature mechanical properties of the $AlMo_{0.5}NbTa_{0.5}TiZr$ alloy, which could help the development of advanced chemically complex alloys.

1. Introduction

Chemically complex alloys (CCAs) are a class of materials with unique microstructures and properties. They have been studied for the past 20 years because they open a wide range of possible combinations of alloying elements with high concentrations that can satisfy the ever-growing requirements of, *e.g.*, high-temperature materials, as conventional one-element-based materials reach their limits [1,2]. Refractory (r)CCAs, which were first reported by Naka [3], contain high concentrations of elements such as Mo, Nb, and Ta and have been widely studied in recent years as a possible solution to the limitations of conventional alloys [4–6], *e.g.*, as potential candidates for improving the efficiency of components used in high-temperature structural applications such as gas turbines [7–9]. One promising example of rCCAs is the $AlMo_{0.5}NbTa_{0.5}TiZr$ alloy (here, the Mo and Ta mol fractions are half those of Al, Nb, Ti, and Zr, corresponding to $Al_{20}Mo_{10}Nb_{20}Ta_{10}Ti_{20}Zr_{20}$ in at%), which was produced for the first time by Senkov et al. [10] and has been replicated and later studied by other authors [11–14]. After cooling from 24 h at 1400 °C, this rCCA decomposes spinodally into a dual-phase A2/B2 (*Strukturbericht* designation [15]) microstructure, also known as α/α' microstructure in Fe-based alloys [16], which resembles the γ/γ' microstructure of well-known Ni-based superalloys [17]. For this reason, together with its good compression properties at room and high temperatures (*i.e.*, yield strength of 2000 MPa and 745 MPa, at 23 and 1000 °C, respectively), this rCCA has also been called refractory superalloy (RSA) by Senkov et al. [10]. It also contains a minor Al-Zr-rich hexagonal intermetallic phase decorating the grain boundaries. The A2/B2 microstructure has also been reported for other CCAs that also form by spinodal decomposition [18].

While its compressive strength is high, the ductility of this RSA and other bcc-based rCCAs [19] is still a great concern. Some efforts have already been undertaken to reduce the room-temperature (RT) brittle behavior of CCAs [20–23], and of the RSA [24]. For example, Soni et al. [25] demonstrated that the RT ductility of the $Al_{0.5}NbTa_{0.8}Ti_{1.5}V_{0.2}Zr$ A2/B2-structured alloy can be improved through phase inversion by controlling the annealing process. Recently, Dong et al. [22] reported that replacing Ta with Ti increases

* Corresponding author.
E-mail address: patricia.suarez-ocano@bam.de (P. Suárez Ocaño).

https://doi.org/10.1016/j.jallcom.2023.169871

the ductility of the $Al_5(NbTaTiZr)_{95}$ alloy, although it may compromise the compressive yield strength. In the case of the $AlMo_{0.5}NbTa_{0.5}TiZr$ RSA, reducing the Mo content also reduces the brittle behavior under compression at RT, although it decreases the strength of the alloy and leads to the formation of a finer Al-Zr-rich phase at grain boundaries [24]. Due to this limitation, the quest to optimize the composition of these alloys and/or to establish new processing routes to improve their properties continues.

Recent studies in the field of CCAs demonstrate that their microstructures and their resulting mechanical properties could be tuned by adjustments of the processing route [26–28]. For instance, Wang et al. [29] determined that an increase in the amplitude of ultrasound solidification refined the $L1_2$/B2 eutectic microstructure and therefore improved the strength and ductility of the $FeCoNi_2Al_{0.9}$ alloy. Cooling rates can have a significant effect on the microstructure and mechanical properties of Ni- and Co-based superalloys [30,31] and of CCAs [32,33], *e.g.*, Munitz et al. [34] demonstrated that changes in the heat treatments and cooling rates lead to microstructural changes of the $AlCrFeNiTi_{0.5}$ CCA, *i.e.*, heat treatment at 650 °C increased the amount of A2/B2 phases and decreased the amount of the ductile fcc phase, thus increasing the hardness but reducing the ductility. In the $Al_{0.5}CoCrFeNi$ CCA, consisting of fcc, bcc and B2 phases, Xoing et al. [35] found that faster cooling rates resulted in larger volume fractions of the B2 phase, which in turn promoted the hardness at the expense of ductility. While these studies suggest that higher cooling rates generally result in higher strength and lower ductility, the specific results may depend on the nature of the alloy.

Given these recent studies that show the potential for modifying the microstructure and mechanical properties of CCAs by controlling their processing routes, the effects of the cooling rate on the microstructure and room temperature mechanical properties of the $AlMo_{0.5}NbTa_{0.5}TiZr$ RSA are investigated here. Specifically, this study focuses on following the microhardness, nanohardness and fracture toughness of the alloy as a function of cooling rate (5, 10 and 30 °C/min).

2. Materials and methods

2.1. Material

Pure elements were vacuum arc melted under Ar atmosphere and allowed to solidify to produce an ingot of approximately 20 × 20 × 50 mm^3. For details related to arc melting, the reader may refer to Ref. [13]. The ingot was subsequently homogenized at 1400 °C for 24 h (under Ar, purity > 99.998 %) and cooled at < 4 °C/min. Then, three slices with dimensions 20 × 20 × 6 mm^3 were individually HIPed (Quintus QIH-9 URQ from Quintus Technologies AB equipped with a Molybdenum furnace) at 1370 °C for 4 h under 170 MPa to close porosity introduced *via* casting, after which each slice was cooled at a different rate of 5, 10, and 30 °C/min. The cooling rate was controlled by natural cooling (free convection) in combination with regulated gas flow of cold gas and heating intervals while the temperature was monitored with 4 thermocouples. Thus, it was possible to control the cooling rates. After processing, metallographic specimens were ground using SiC abrasive papers (p320, p600, p1200, p2500, and p4000) followed by polishing for 10 min using colloidal silica with a 50-nm grain size.

2.2. Mechanical properties

Nano and microindentation tests at RT were conducted on the metallographically prepared specimens that underwent different cooling rates (5, 10, and 30 °C/min). While the microhardness tests were averaged over several phases and grains of the matrix, 10–16 local nanoindentation tests were performed to evaluate the nanohardness of intermetallics forming at grain boundaries and two-phase (A2/B2) regions within grains. The nanoindentation measurements were performed using a Hysitron TriboIndenter (Hysitron TI 980 Bruker) equipped with a Berkovich diamond indenter tip, a maximum load of 8 µN, a holding duration of 10 s, and a speed of 0.8 µN/s. The displacement (h) was monitored as a function of the load (P) throughout each load-unload cycle. The indentation modulus E_r was determined from the slope of the unloading curve at maximum load using the classical relationship [36]:

$$E_r = \frac{1}{2}\frac{\sqrt{\pi}}{\sqrt{A}}\frac{dP}{dh} \quad (1)$$

The elastic (Young's) modulus (E) of the alloy can then be calculated from [37]:

$$\frac{1}{E_r} = \frac{1-\nu^2}{E} + \frac{1-\nu_i^2}{E_i} \quad (2)$$

where ν (assumed to be equal to 0.3) and ν_i (= 0.07) are the Poisson's ratios of the specimen and diamond indenter tip, respectively, and E_i represents the Young's modulus of the indenter tip (E_i = 1141 GPa [38]).

Microhardness measurements were performed following the DIN EN ISO 6507-2 standard with a testing machine (KB 30 SR FA Basic) equipped with a Vickers indenter tip. Measurements were performed with three different weights of 1, 20, and 30 kg (loads of 9.8 N, 196 N, and 294 N, respectively) and about 20 indentations for each load. Subsequently, both diagonals of each remnant indent were measured by optical microscopy to estimate the hardness. To avoid interactions between indents, the latter were performed 2 mm apart. The fracture toughness (K_c) of the RSA was estimated using the model described in Ref. [39]. To this end, the lengths of the cracks formed at the corners of the indenter tip were measured using a scanning electron microscope (SEM) equipped with a field emission gun (FEG) and a backscatter electron detector (BSE) at an acceleration voltage of 25 kV (SEM, FEI Quanta 3D). First, only remnant indents whose four primary cracks emanated straight and radially from each corner (as described in the ISO 21618 standard [40]) were considered. Then, indents with spalled edges, asymmetrical, split, or forked cracks were also considered to compare the final values between the subset and the full set of microindents. SEM images were acquired in the specimens after microhardness testing with 20 and 30 kg. Additionally, the fraction of cracks, F_c, at the corners of the indents was determined using F_c = total number of cracks / (number of indents × 4). To make a comparison of the fracture toughness of the RSA with different relevant engineering materials, including bcc-structured alloys, an Ashby plot was generated using the GRANTA Edupack software (ANSYS, Inc.), which shows the fracture toughness as a function of Vickers microhardness.

2.3. Characterization

The microstructures of the specimens cooled under different conditions were analyzed before mechanical testing using the previously mentioned SEM. The latter is equipped with an energy-dispersive X-ray spectroscopy (EDS, EDAX Octane Elect SDDs) detector that allowed for determining the compositions of different phases and two-phase regions. The average grain size was determined according to ASTM E112 [41]. SEM-EDS analyses of large regions (≈ 2 mm^2) were performed on the three specimens cooled at 5, 10, and 30 °C/min (see Table S1 of Supplementary Material). Table 1 shows the average chemical composition of the $AlMo_{0.5}NbTa_{0.5}TiZr$ RSA.

For transmission electron microscopy (TEM), samples were prepared as described elsewhere [13]. Conventional (C)TEM was used to acquire selected area diffraction patterns (SADPs), bright-field (BF), and dark-field (DF) micrographs. Scanning (S)TEM was conducted

Table 1
Chemical composition of the RSA obtained using semi-quantitative SEM-EDS averaged over large regions. All concentrations are in at%.

	Al	Mo	Nb	Ta	Ti	Zr
Concentrations in at%	22	12	20	8	20	18

using the high-angle annular (HAA)DF mode for atomic number contrast imaging (*Z*-contrast). The TEM (JEOL JEM-2200FS), equipped with a FEG, was operated at an acceleration voltage of 200 kV.

The size of the bcc (A2) precipitates, and B2 channels, as well as the area fractions of the present phases in the HIPed samples after different cooling rates, were estimated using the image analysis package FIJI [42].

X-ray diffraction (XRD) patterns were recorded at RT, 200, 600, 800, and 900 °C with a D8 Advance Bruker diffractometer using the Bragg–Brentano geometry, a Cu Kα1 radiation ($\lambda_{K\alpha1}$ = 0.15406 nm), and a 2θ scattering range between 10° and 140°. For the high-temperature measurements, an Anton Paar furnace under vacuum (≈ $5{\cdot}10^{-2}$ mbar) was employed. The identification of the phases was carried out by comparing the experimental patterns with simulated patterns using the PowderCell software package [43]. The lattice parameters of the different phases were determined from the peak positions (2θ) in combination with Bragg's law.

The temperature dependence of the lattice parameters and the misfit between the A2 and B2 phases were additionally calculated using the ThermoCalc software (version 2020b) [44] in combination with the TCHEA3 database. For this purpose, the molar volumes (V_m) of the A2 and B2 phases were calculated as a function of temperature and the corresponding lattice parameters (a) were deduced from:

$$a = \left[\frac{2V_m}{N_A}\right]^{\frac{1}{3}} \quad (3)$$

where V_m is the molar volume and N_A is the Avogadro's constant. The lattice misfit δ in % was subsequently determined from a_{A2} and a_{B2} using Eq. (4):

$$\delta = \frac{2(a_{A2} - a_{B2})}{a_{A2} + a_{B2}} 100 \quad (4)$$

3. Results and discussion

3.1. Effect of the cooling rate on the A2/B2 microstructure after HIP

Fig. 1 shows the microstructure of the RSA at different magnifications for the specimens cooled at 5 °C/min (1st column), 10 °C/min (2nd column), 30 °C/min (3rd column). The microstructure in the three cases consists of equiaxed grains (first row of Fig. 1) containing subgrain boundaries. Grain and subgrain boundaries are marked with blue and red arrows, respectively, in the second row of Fig. 1. The average grain size is found to be nearly independent of cooling rate, *i.e.*, 151 ± 32 µm for 5 °C/min, 147 ± 26 µm for 10 °C/min, and 154 ± 25 µm for 30 °C/min. This shows that the three specimens experienced similar thermal histories and the region of the ingot from where they were extracted had a homogeneous grain size. At low magnification, contrast variations are visible within grains, indicating that the dendritic microstructure was not fully homogenized during our heat treatment (1400 °C for 24 h).

In the 5-°C/min sample (Fig. 1a), the grain boundaries are almost completely covered by dark precipitates surrounded by a bright rim (Fig. 1b). They occupy 7 ± 1 % of the surface (see Fig. S1 of supplementary material and Table 2 and were identified in previous studies as a hexagonal Al-Zr-rich phase ($Al_{4-x}Zr_5$, with $0 \le x \le 1$) with a $P6_3/mcm$ space group while the bright regions surrounding the precipitates correspond to a Nb-Mo-Ta-rich A2 phase (< 1 %) [10,11,13]. These phases were also identified in the sample cooled at 10 and 30 °C/min, but the area fractions of the Al-Zr-rich phase were 3 ± 1 % and < 1 %, *i.e.*, 2.3 and 7 times lower than in the 5-°C/min specimen, respectively (Fig. S1 and Table 2). Based on this observation, it can be concluded that a lower cooling rate promotes the precipitation of the Al-Zr-rich phase. When the cooling rate is sufficiently slow, Al and Zr diffuse towards grain boundaries and allow the Al-Zr-rich phase to grow while Ti, Ta, and Nb diffuse in the opposite direction and accumulate at the rim of these intermetallic particles. Note that the amount of the Al-Zr-rich phase is disputed in the literature. For the same heat treatment (1400 °C for 24 h) and cooling rate (10 °C/min), three different area fractions were reported for the Al-Zr-rich phase, *e.g.*, Jensen found 16 % [45], Senkov et al., 6 % [10] and Whitfield et al. less than 1 % [12]. This discrepancy cannot be solved at this point.

At higher magnification (3rd row of Fig. 1), the well-known nanostructure described previously [10,24] with aligned cuboidal A2 precipitates embedded in a continuous B2 matrix appears for the three different cooling rates. However, the cooling rate is found to strongly affect the length scale of the nanostructure: the greater the cooling rate, the finer the nanostructure.

Due to their small size, the A2 precipitates were further characterized by TEM. Fig. 2a-c show CTEM-DF micrographs and corresponding SADPs of the 5, 10, and 30-°C/min specimens, respectively, viewed along the [001] zone axis. By selecting the superlattice reflection (100) marked with green circles in the SADPs (shown as insets), the ordered B2 channels appear bright while the disordered A2 precipitates are dark. A more detailed analysis of the CTEM-DF micrographs is provided in Figs. S2-S4 of the supplementary material. The contrast in the STEM-HAADF micrographs in Fig. 2d-f is equivalent to the BSE contrast in Fig. 1a-c but with a better resolution, *i.e.*, the A2 precipitates appear brighter than the B2 matrix owing to their higher *Z*-contrast. SEM-EDS and TEM-EDS analyses in Table S2 of supplementary material confirmed that the A2 phase is Mo-Nb-Ta-rich while the B2 phase is Al-Zr-rich and the hexagonal $P6_3/mcm$ phase is Al-Zr-rich, consistent with previous reports on the $AlMo_{0.5}NbTa_{0.5}TiZr$ RSA [10,24]. The diffraction contrast in the STEM-BF images did not reveal the presence of dislocations at the A2/B2 interfaces after cooling from 1370 °C (see Fig. S5 and Fig. S6 of supplementary material), so that all the aligned cuboidal precipitates were fully coherent unless found at defective regions, *e.g.*, subgrain boundaries (see red arrows in Fig. 1b, e and h), which were not quantified here.

The relative area fractions of the A2 and B2 phases were determined from STEM-HAADF micrographs (see Fig. S7 of supplementary material). The mean grain size, the area fractions of the different phases, the range of precipitate and channel sizes as well as their average sizes for the RSA cooled at different rates are summarized in Tables 2 and S3. It is also visible in Fig. 2d-f that the B2 phase presents narrow and wide channels, whose widths are provided in Table 2.

The variations in area fractions of the A2 and B2 phases after different cooling rates (*cf.* Table 2) are small compared to the error bars, indicating that they are approximately independent of cooling rates. In contrast, the average edge length (d) of the A2 precipitates and the width of the wide B2 channels significantly decrease by 36 % and 61 % with increasing cooling rates from 5° to 30°C/min, respectively (*cf.* Table 2). At this point, d disregards the elongated character of the A2 precipitates. This aspect is now investigated in more detail in Fig. 3, which shows the aspect ratio (AR) histograms of the A2 precipitates in the RSA cooled at different rates. The AR of each precipitate is calculated as: AR = narrow edge length / wide edge length, with $0 \le AR \le 1$, so that the projection of the particle is an almost perfect square when AR is close to 1. These projected square-shaped particles are mostly located at the intersections of

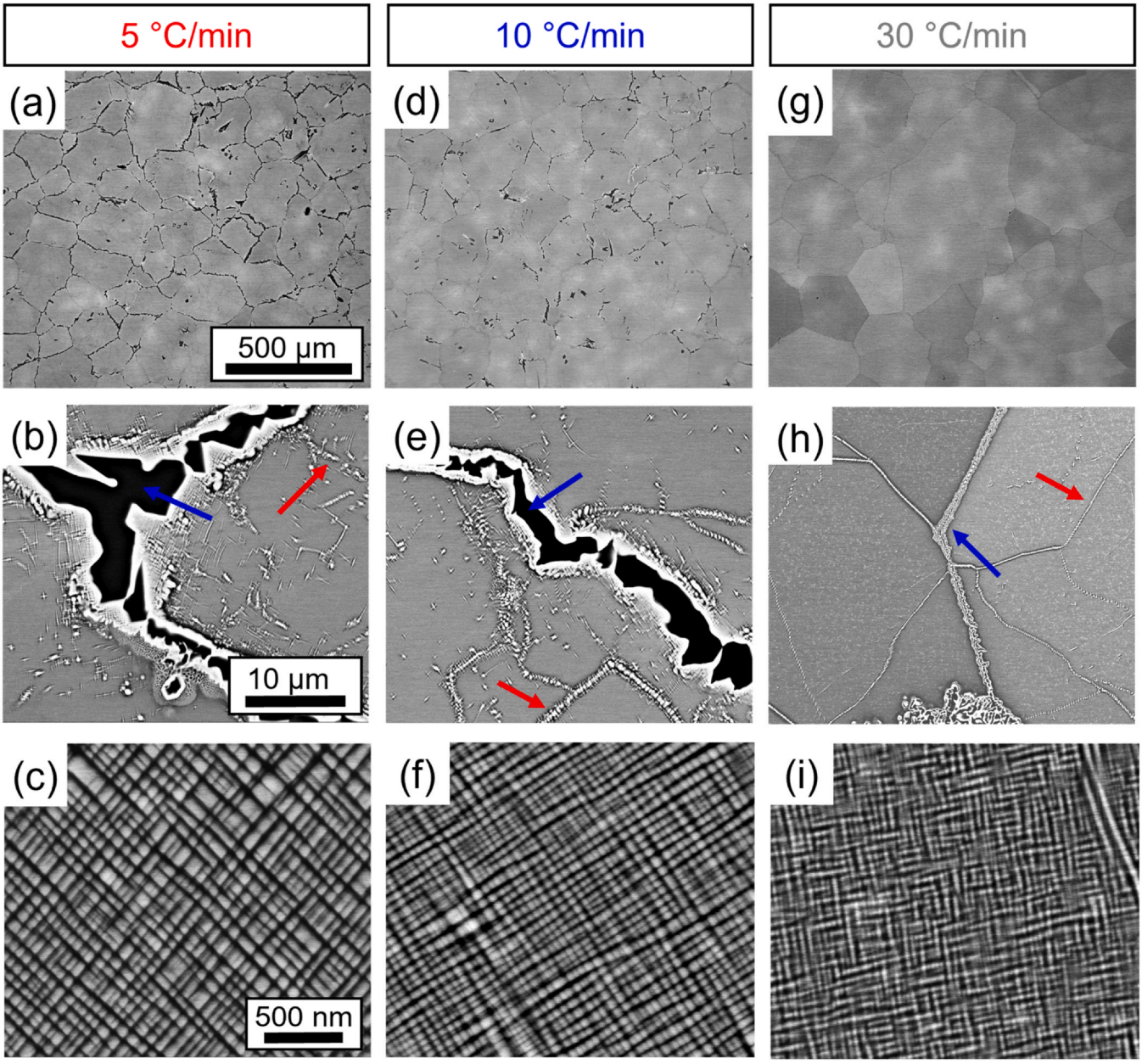

Fig. 1. BSE micrographs of the RSA after annealing (1400 °C for 24 h) followed by HIP (1370 °C for 4 h at 170 MPa) and cooling at (a-c) 5 °C/min, (d-f) 10 °C/min, and (g-i) 30 °C/min. Note that the magnification within a given row is the same. The blue and red arrows indicate grain and subgrain boundaries, respectively.

Table 2
Grain size, area fractions of the different phases, edge length of the A2 precipitates, and width of the B2 channels in the RSAs cooled at different rates. The error bars correspond to the standard deviations.

Cooling rate (°C/min)	Grain size (μm)	Phase area fraction (%)			Phase average size (nm)		
		B2 channels	A2 precipitates	$Al_{4-x}Zr_5$, $0 \le x \le 1$	B2 channel width		A2 precipitate edge length (d)
					narrow	wide	
5	151 ± 32	54 ± 7	39 ± 7	7 ± 2	4 ± 1	46 ± 20	25 ± 15
10	147 ± 26	62 ± 2	35 ± 2	3 ± 1	3 ± 1	31 ± 12	18 ± 9
30	154 ± 25	54 ± 4	45 ± 4	< 1	3 ± 1	18 ± 8	16 ± 7

two perpendicular rows of aligned precipitates, *i.e*, each row is delimited by wide channels, Fig. 2d-f. A comparison of Fig. 3a-c reveals that the percentage of A2 particles with a nearly perfect square shape (see black arrows) declines with a decreasing cooling rate, indicating that the elastic strain energy of rows of aligned slabs becomes lower than that of cubes as the particles coarsen. Apart from the sharper maximum at $AR \approx 1$ for higher cooling rates, the AR distribution shows a broad asymmetric maximum. The position of this broad maximum as well as its width are found to increase with an increasing cooling rate. It is thus clear that there is a tendency to form more symmetric precipitates (with higher AR values) in the RSA as the cooling rate increases. Note that the composition of the

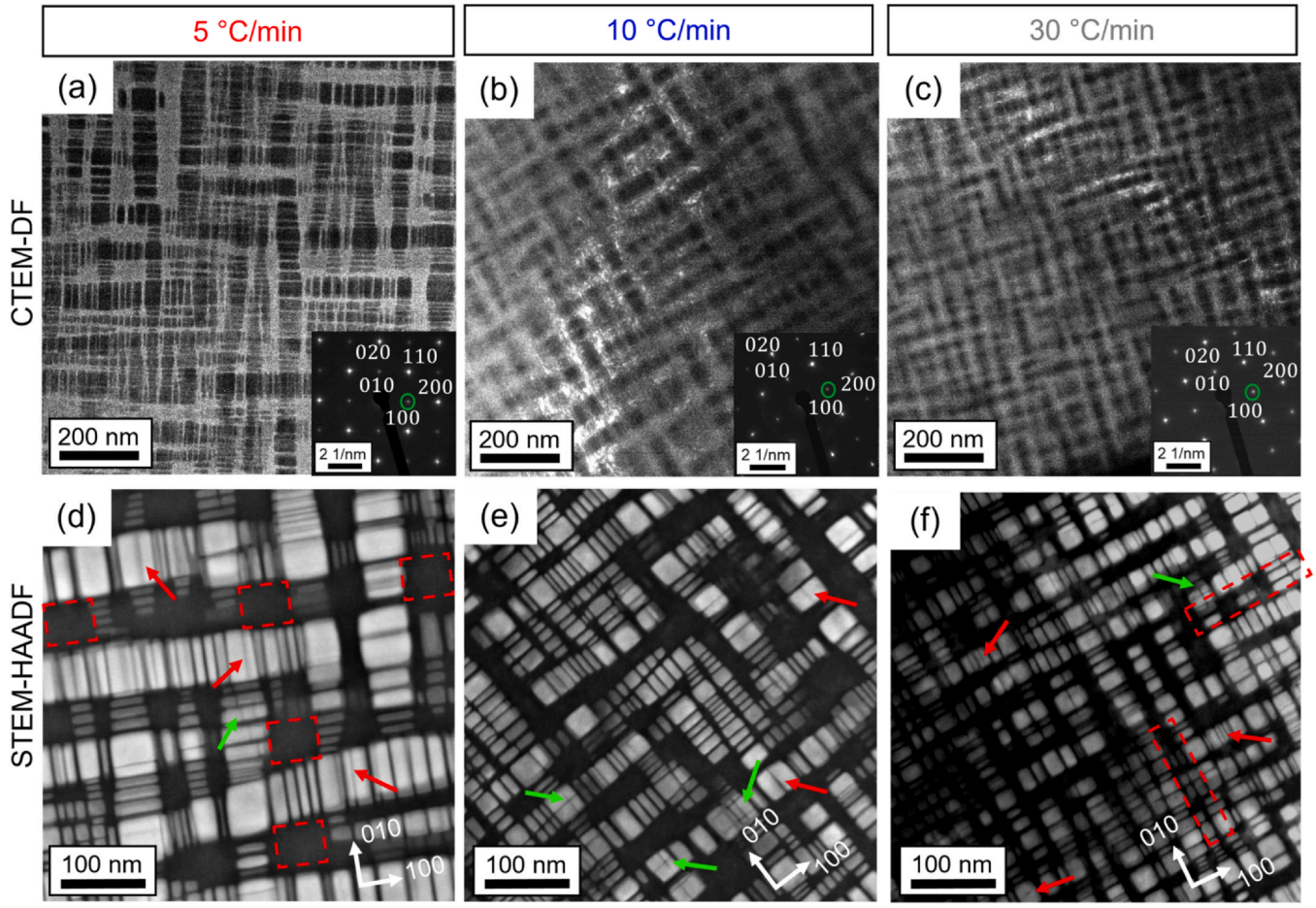

Fig. 2. (a–c) CTEM-DF micrographs of the nanostructure within equiaxed grains oriented along the [001] zone axis with their respective SADPs (insets) for RSAs cooled after HIP at (a) 5 °C/min, (b) 10 °C/min, and (c) 30 °C/min. Superlattice reflections (100) used for imaging are marked with green circles. In this diffraction condition, the B2 phase appears bright while the A2 phase is darker. (d–f) Equivalent STEM-HAADF micrographs for (d) 5 °C/min, (e) 10 °C/min, and (f) 30 °C/min. The fact that the contrast of the A2 slabs and cubes is brighter in (d-f) indicates that these precipitates have a higher density than the B2 matrix. The red and green arrows in Fig. 2d-f, and red dashed rectangles in Fig. 2d and f, represent a comparison with the mechanisms proposed by Wang et al. [46]. For details see Section 3.4 and Fig. 7.

A2 and B2 phases remains approximately the same in all three states, as determined with TEM EDS (Table 3).

Based on these results, it can be concluded that the cooling rate affects the microstructure of the RSA in terms of morphology, size, and distribution of both B2 channels and A2 precipitates, as well as the precipitation of the Al-Zr-rich phase. The area fractions of B2 and A2 phases fluctuate around rather constant values and the width of the thin B2 channels remains roughly constant.

As shown previously, a slow cooling rate promotes the heterogeneous precipitation of an Al-Zr-rich phase at grain boundaries. Since this phase grows at the expense of the B2 phase [22], one may expect the B2-phase volume fraction in the vicinity of grain boundaries to be locally lower. However, since the area fractions and compositions of the A2 and B2 phases (*cf.* Table 3) were determined in the center of the grains, their values are unlikely to be affected by the presence of the Al-Zr-rich phase. This may be the reason why the area fractions and compositions of the A2 and B2 phases listed in Table 3 do not significantly depend on the cooling rate.

3.2. Effect of cooling rate on the lattice misfit

The XRD patterns at RT of the RSA cooled at 5, 10, and 30 °C/min are displayed in Fig. 4 as black, light and dark purple lines, respectively. The A2 and B2 phases as well as a hexagonal $Al_{4-x}Zr_5$ intermetallic were identified. The lattice parameters of these phases (see Tables 3 and 4) agree well with those previously determined for the $AlMo_{0.5}NbTa_{0.5}TiZr$ RSA [10,12,13,45]. The lattice misfit, δ, between the A2 and B2 phases was calculated using Eq. (4) [48], resulting in negative lattice misfits (Table 4).

As the lattice parameters of the hexagonal intermetallic phase were found to be nearly independent of the cooling rate, we provide their average values in Table 4. In contrast, when the cooling rate increases, the lattice parameters of the A2 and B2 phases in Table 4 increase and decrease respectively, resulting in a decreasing magnitude of the apparent lattice misfit. In principle, there are three potential contributions to this evolution, namely (1) the formation of a dislocation network at the A2/B2 interface that may relax the misfit (resulting in stronger differences between a_{A2} and a_{B2}), (2) a change in the composition between the A2 and B2 phases, and (3) a size effect related to the density of A2/B2 interfaces. (1) As no dislocations were observed by TEM at the A2/B2 interfaces regardless of the cooling rate (*cf.* Fig. S5 and Fig. S6 of the supplementary material), we conclude that the investigated cooling rates are fast enough to avoid the formation of dislocations upon cooling. Therefore, this contribution can be neglected. (2) TEM-EDS observations (*cf.* Table 3) show that the composition of the A2 and B2 phases does not change significantly with the cooling rate. A contribution of the composition on the lattice misfit can thus be ruled out. (3) When the cooling rate is slow, there is a low number density of large precipitates. As the lattice misfit across a coherent interface induces an elastic strain [49], the lattice parameters of the A2 and B2 phases in the vicinity of the interface are constrained, resulting in a small local "constrained"

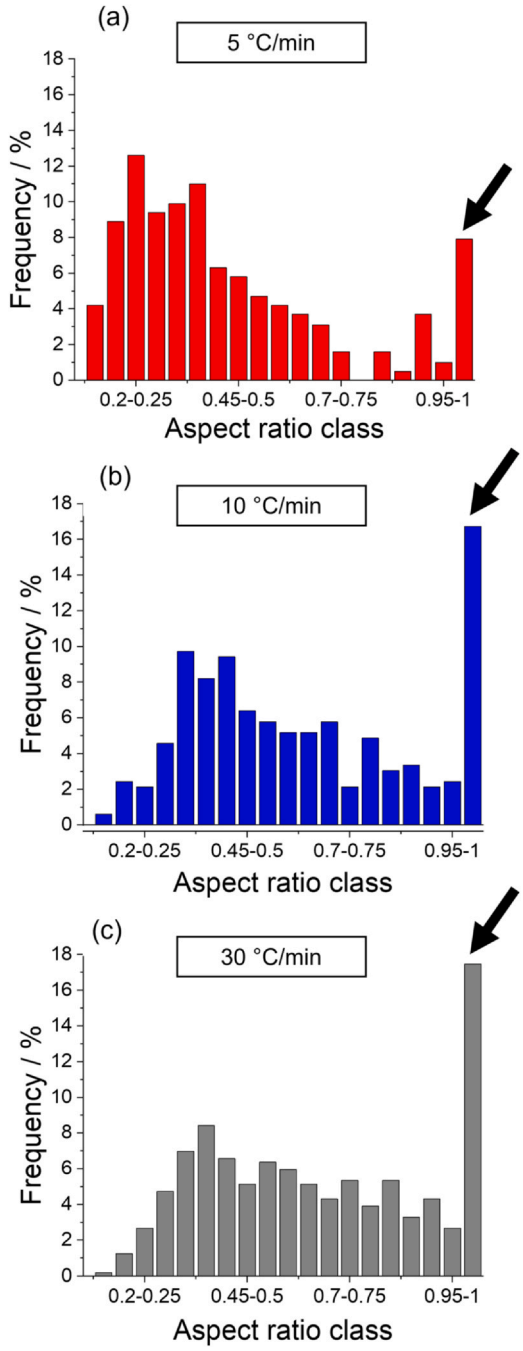

Fig. 3. Histograms showing the relative frequency distributions of A2-particles aspect ratios in the RSAs cooled at (a) 5 °C/min, (b) 10 °C/min, and (c) 30 °C/min.

misfit. However, these constraints are progressively relaxed as one moves away from an interface. As a result, the cores of the large A2 precipitates and wide B2 channels are less affected by the coherency misfit and the local apparent misfit is larger there. When there is a high number density of small precipitates (*e.g.,* for a high cooling rate), the density of A2/B2 interfaces is larger, resulting in a greater effective volume affected by elastic strains and therefore the magnitude of the apparent macroscopic lattice misfit is smaller. This latter contribution is in line with our experimental results in Table 4.

Now we compare our results with those reported in the literature. All recorded A2/B2 lattice misfits of the $AlMo_{0.5}NbTa_{0.5}TiZr$ RSA at RT are between − 1 and − 2%. (*cf.* Table 3). Compared to δ in *fcc*-structured superalloys, which are usually in the order of − 0.1 % (in many commercial Ni-based superalloys) or + 0.3 % (Co-base) [50], the misfit value in the $AlMo_{0.5}NbTa_{0.5}TiZr$ RSA is very large. A detailed comparison of our lattice misfit data with the works from Senkov et al., ($\delta = -1.1$ % [10]), Kloenne et al. ($\delta = -2.1$ % [14]) and Whitfield et al. ($\delta = -1.51$ % [12]) proves challenging on different levels, *e.g.*, the uncertainty of some of those measurements was either not given [12], or led to variations of up to $\Delta\delta = 0.6$ % [10], albeit, in the latter case, the authors did not focus on the subject of lattice misfit. In two of the works summarized in Table 3 [10,12], the final microstructure arose after cooling from 1400 °C at 10 °C/min, while in the work by Kloenne et al. [14], the lattice misfit was studied after aging at 1000 °C for 6 h and subsequent water quenching (*cf.* Table 3).

The work of Senkov et al. [10] reported $|\delta| \approx 1.07$ %. If we use the measurement uncertainty given by Senkov et al. to find the lower and higher limits for their a_{A2} and a_{B2} and apply Eq. 4, we find the range $-1.37\ \% < \delta < -0.76\ \%$ (*cf.* 4th row in Table 3). The a_{A2} and a_{B2} values reported by Whitfield et. al. [12] (*cf.* 5th row in Table 3) yield $\delta \approx -1.51$ %. They did not report an uncertainty for the measurements. However, their δ is more negative than that of Senkov et al. [10], and thus closer to what we found. Considering the three possible contributions to the lattice misfit mentioned previously, we can state the following: (1) the A2/B2 images reported by Senkov et al. [10] (*cf.* their Figs. 5 and 6) do not show the presence of misfit dislocations, as in our case. The SEM images reported by Whitfield et al. [12] reveal an A2/B2 microstructure with flat interfaces and sharp corners resembling our dislocation-free interfaces. (2) The chemical composition of Senkov's A2 and B2 phases is similar to ours (Table 3) but no information on A2 and B2 compositions was reported by Whitfield et al. [12]. (3) By inspection of the (S)TEM images from Senkov et al. [10] and from their stated values, both the average edge length of their A2 precipitates and the width of their wide B2 channels are smaller than our measured values. They report a higher fraction of the A2 phase than we do. These values would represent an increased density of A2/B2 interfaces in their material state, which in turn would lead to a stronger constrain of the respective inner phase regions by the latter, and thus to a smaller value of $|\delta|$. As for a comparison with the work by Whitfield et al. [12], no conclusion can be drawn because their SEM-BSE image does not show the widths of the channels precisely enough.

In the third work, Kloenne et al. [14] used a different material condition: their alloy was aged at 1000 °C for 6 h and water quenched. After aging, the authors found that an array of misfit dislocations formed at the A2/B2 interfaces to relax the coherency strains. Based on the spacing between dislocations, Kloenne et al. [14] estimated a "relaxed" lattice misfit of − 2.1 %, which is more negative than our "constrained" values for fully coherent A2/B2 interfaces.

3.3. Temperature dependence of the lattice misfit δ

To determine the temperature-dependent lattice parameters of the A2 and B2 phases, as well as the lattice misfit between them, *in-situ* XRD was performed between RT and 900 °C in an RSA that was cooled at 10 °C/min. The *in-situ* XRD patterns are shown in Fig. 5 where the inset allows us to distinguish the 110 peaks of the A2 and B2 phases. At RT, the A2 and B2 peaks are clearly separated. With increasing temperature, the intensity of the 110 peaks of the A2 phase decreases due to its progressive dissolution. Moreover, the distance between the 110 peaks of the A2 and B2 phases decreases between RT and 900 °C, indicating that the difference between the lattice parameters decreases. From the XRD patterns in Fig. 5, the obtained lattice parameters (a_{A2} and a_{B2}) and the lattice misfit are summarized in Table 5 and their temperature dependences are shown on the left and right axes of Fig. 6a, respectively. With increasing temperature from RT to 200 °C, as the atomic mobilities are extremely low, the microstructure must remain constant and the changes in a_{A2} and a_{B2} reflect thermal expansion. In Fig. 6a, a_{A2} is

Table 3
Phases, compositions, microstructural features, and processing parameters of the $AlMo_{0.5}NbTa_{0.5}TiZr$ RSA from this work and other studies. The phase and alloy compositions were determined by TEM-EDS and SEM-EDS, respectively. In this table, we also list the area fractions (*AF*) of the different phases, the lattice parameters of the cubic phases, the lattice misfit (δ) between the A2 and B2 phases, the A2/B2 coherency, the corresponding heat treatments, and sources.

Phase / alloy	Concentration (at%)						*AF* (%)	*a* (Å)	δ (%)	A2/B2 coherency	(Final heat treatment step) cooling◊	Source
	Al	Ti	Zr	Mo	Nb	Ta						
A2	5 ± 1	17 ± 1	8 ± 1	17 ± 1	30 ± 1	23 ± 1	39	3.2632	−1.65 > δ > −1.77	Fully coherent	(1370 °C, 4 h) 5 °C/min	This work
B2	27 ± 1	23 ± 1	25 ± 1	8 ± 1	13 ± 1	4 ± 1	54	3.3196				
$Al_{4-x}Zr_5$	40 ± 1	9 ± 2	34 ± 1	3 ± 1	11 ± 1	2 ± 1	7					
alloy	22	20	18	12	20	8						
A2	4 ± 1	15 ± 1	11 ± 1	17 ± 1	29 ± 1	24 ± 1	35	3.2616	−1.54 > δ > −1.73	Fully coherent	(1370 °C, 4 h) 10 °C/min	This work
B2	26 ± 1	21 ± 1	25 ± 1	9 ± 1	14 ± 1	5 ± 1	62	3.3155				
$Al_{4-x}Zr_5$	39 ± 1	9 ± 1	34 ± 1	4 ± 1	11 ± 1 20	3 ± 1	3					
alloy	23	20	18	12		7						
A2	5 ± 1	16 ± 1	10 ± 1	16 ± 1	27 ± 1	26 ± 1	45	3.2616	−1.20 > δ > −1.52	Fully coherent	(1370 °C, 4 h) 30 °C/min	This work
B2	27 ± 1	22 ± 1	24 ± 1	8 ± 1	14 ± 1	5 ± 1	54	3.3155				
$Al_{4-x}Zr_5$	40 ± 1	9 ± 1	35 ± 1	3 ± 1	10 ± 1	3 ± 1	< 1					
alloy	22	21	17	12	20	8						
A2	4	17	10	16	32	22	45	3.2690	−0.76 > δ > −1.37	Fullycoherent	(1400 °C, 24 h) 10 °C/min	[10,45]
B2	26	25	26	6	14	4	39	3.3040				
$Al_{4-x}Zr_5$●	37	10	38	3	9	3	16	(±0.005)				
alloy	20	18	19	11	22	10						
A2	18	21	22	9	19	11	50	3.2700	−1.51♠	Fully coherent	(1400 °C, 24 h) 10 °C/min to 750 °C + furnace cooled	[12]
B2							50	3.3200				
$Al_{4-x}Zr_5$●							< 1					
alloy												
A2	12	20	9	15	28	16	♦Same as	3.3100	−2.00 > δ > −2.19	Relaxed by misfit dislocations	(1000 °C, 6 h) Water quench	[14,47]
B2	30	25	24	6	12	3	Senkov	3.3800				
$Al_{4-x}Zr_5$●							et al.[10]					
alloy												

♠ Calculated using Eq. 4, from values of lattice parameter described in [12]
◊ All works treated the alloy to 1400 °C for 24 h before final cooling step
• For simplification, we assume that the Al-Zr-rich phase, reported by other authors, corresponds to our $Al_{4-x}Zr_5$ phase.
♦ Assumption based on provision of material by O. Senkov, as stated in their acknowledgement [14].

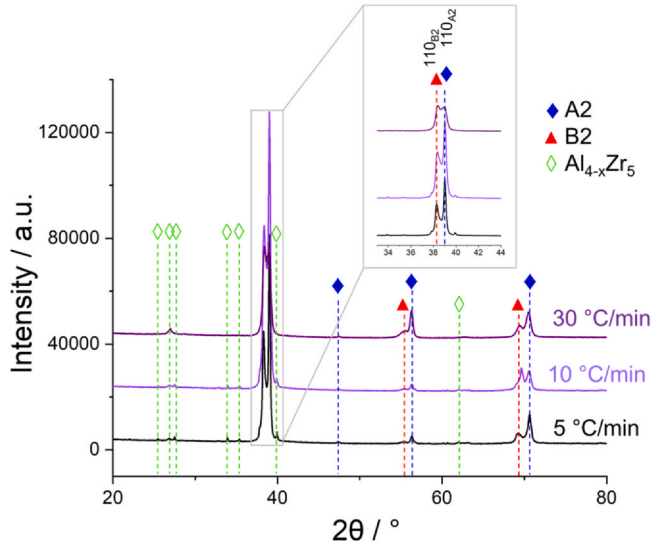

Fig. 4. XRD patterns of the RSA cooled at 5 °C/min (black), 10 °C/min (light purple), and 30 °C/min (dark purple). The (110) reflections of the A2 and B2 phases are magnified in the inset. The dashed lines represent the position of the peaks in the sample cooled at 5 °C/min for the A2 (blue), B2 (red), and $Al_{4-x}Zr_5$ (green) phases.

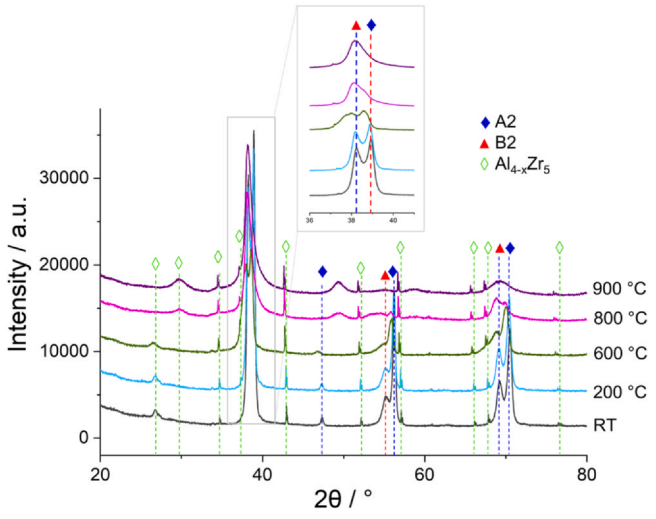

Fig. 5. *In-situ* XRD patterns of the 10-°C/min sample at different temperatures (RT, 200, 600, 800, and 900 °C). The dashed lines represent the position of the peaks in the sample at RT for the A2 (blue), B2 (red), and $Al_{4-x}Zr_5$ (green) phases. As the temperature increases, the thermal expansion induces a peak shift towards lower angles.

Table 4
Lattice parameters of the A2 and B2 phases (a_{A2} and a_{B2}) determined by XRD in the samples cooled at different rates and corresponding apparent lattice misfits. Also shown are the lattice parameters (*a*, *c*) of the Al-Zr-rich hexagonal phase. The uncertainties in "*a*", associated with the fit of the 2θ peaks in the A2/B2 phases, are given by the standard deviation of several peaks for the $Al_{4-x}Zr_5$ phase and are calculated by the laws of error propagation for the lattice misfit.

	Lattice parameters (Å)			Lattice misfit δ (%)
Cooling rate	a_{A2}	a_{B2}	$Al_{4-x}Zr_5$, $0 \le x \le 1$	
5 °C/min	3.2632 ± 0.0006	3.3196 ± 0.0010	a = 8.0565 ± 0.0063	-1.71 ± 0.06
10 °C/min	3.2616 ± 0.0009	3.3155 ± 0.0016	c = 5.4504 ± 0.0119	-1.64 ± 0.09
30 °C/min	3.2689 ± 0.0033	3.3138 ± 0.0019		-1.36 ± 0.16

found to increase at a slightly higher rate than a_{B2} with increasing temperature from RT to 200 °C, thus resulting in an increase of the misfit, which becomes less negative. These variations can be explained as follows: as the atoms in an ordered intermetallic are more strongly bonded compared to a disordered solid solution with the same structure, the binding energy-*vs.*-distance curve of the B2 phase is expected to be narrower than that of the A2 phase. Therefore, the former should have a lower coefficient of thermal expansion than the latter [51], consistent with our experimental results and those reported in the field of Ni-based superalloys [52].

Between 200 and 600 °C, δ strongly increases from − 1.54 ± 0.05 to − 1.23 ± 0.27 (see Table 5). As atomic mobilities become sufficiently large at 600 °C, diffusion becomes significant and allows microstructural changes. At 600 C, the driving force for A2 precipitation must be large and we believe that nanoscale A2 precipitates may form within the B2 channels, similar to the precipitation of tertiary γ' typically observed in Ni-based superalloys in this temperature range [17,53]. However, further work is still required to confirm or discard this hypothesis.

When the temperature is further increased between 600 and 900 °C, δ continues to increase probably due to thermal expansion and an eventual change of the A2 and B2 compositions.

Using Thermo-Calc in combination with the TCHEA3 database, we also computed the evolutions of a_{A2}, a_{B2}, and δ by changing the temperature, the effects of which are shown with gray, black, and red lines in Fig. 6b, respectively. Here, the colored backgrounds indicate the temperature domains in which different phases are stable, *e.g.*, A2 + B2 + σ + Al_3Zr_4 in beige. While the σ phase is one of the most commonly reported intermetallics in steels [54,55], Ni-based superalloys [56], HEAs [57] and compositionally complex alloys [20], this phase was not observed in the present work after cooling from high temperatures. Recently, Whitfield et al. [12] performed long-term 1000-h anneals to investigate the phase stability of the $AlMo_{0.5}NbTa_{0.5}TiZr$ alloy between 800 and 1200 °C. The authors reported that the σ phase is not stable in this temperature range, indicating that the TCHEA3 database should be improved to ensure better predictions.

Since ThermoCalc predicts that the A2 and B2 phases are in equilibrium above ≈ 750 °C [13], the dotted beige region between 750 and 900 °C in Fig. 6a,b highlights this temperature range in which the experimental and calculated data can be compared.

The temperature-dependence of the calculated and experimental lattice misfit show opposite trends between 800 and 900 °C (compare red curves in Fig. 6a,b). This may be related to the presence of the σ phase in the thermodynamic calculations, which was not detected experimentally. Furthermore, in the TCHEA3 database, all phases are considered as disordered even though the B2 and Al-Zr-rich phases are ordered intermetallics. That is, ThermoCalc in combination with TCHEA3 computes phase equilibria based only on phase compositions. Another reason for the discrepancies between the ThermoCalc results and our data is that ThermoCalc considers stable states at different equilibrium temperatures after long-term anneals while our samples were continuously cooled at different rates from high temperatures. The *in-situ* experiment, which led to a reduction of the apparent lattice misfit with increasing temperature, took a few minutes at each temperature and the obtained temperature-dependent lattice misfit may thus correspond to metastable states. Therefore, it cannot be directly compared with equilibrium data, nor with the long-term exposure experiment performed by Kloenne *et al.* [14]. Further investigations on long-term exposure are planned for a subsequent investigation. The short hold times in the *in-situ* experiment reflect rather the evolution of the lattice misfit while cooling from 900 °C to RT, which as expected shows a continuous increase in lattice misfit as the temperature is lowered.

Finally, these results demonstrate that a faster cooling rate during solidification can promote the formation of a finer and more homogeneous A2/B2 microstructure in the RSA with a more constrained lattice misfit between the A2/B2 phases.

Table 5
Lattice parameters of the A2 and B2 phases at different temperatures, measured *via in-situ* XRD using the sample cooled at 10 °C/min.

Temperature (° C)	Lattice parameter (Å)		Lattice misfit B2/A2 (%)
	a_{A2}	a_{B2}	δ
RT	3.2616 ± 0.0009	3.3155 ± 0.0016	-1.64 ± 0.09
200	3.2749 ± 0.0006	3.3258 ± 0.0008	-1.54 ± 0.05
600	3.2912 ± 0.0005	3.3319 ± 0.0073	-1.23 ± 0.27
800	3.2979 ± 0.0027	3.3362 ± 0.0016	-1.15 ± 0.11
900	3.2970 ± 0.0036	3.3342 ± 0.0012	-1.12 ± 0.13

3.4. A2/B2 microstructure: origin of narrow and wide B2 channels as well as plate and cubic-shaped A2 precipitates

The A2/B2 microstructure of the $AlMo_{0.5}NbTa_{0.5}TiZr$ RSA was reported to form by spinodal decomposition [10]. Based on experimental observations and phase-field simulations, the specific pathway was later proposed to occur in three steps upon cooling [45,47]: (1) congruent ordering (A2 to B2 phase); (2) spinodal decomposition of B2 into Al-Zr-rich and Mo-Nb-Ta-rich regions; and (3) disordering of Mo-Nb-Ta-rich B2 regions to A2, which form

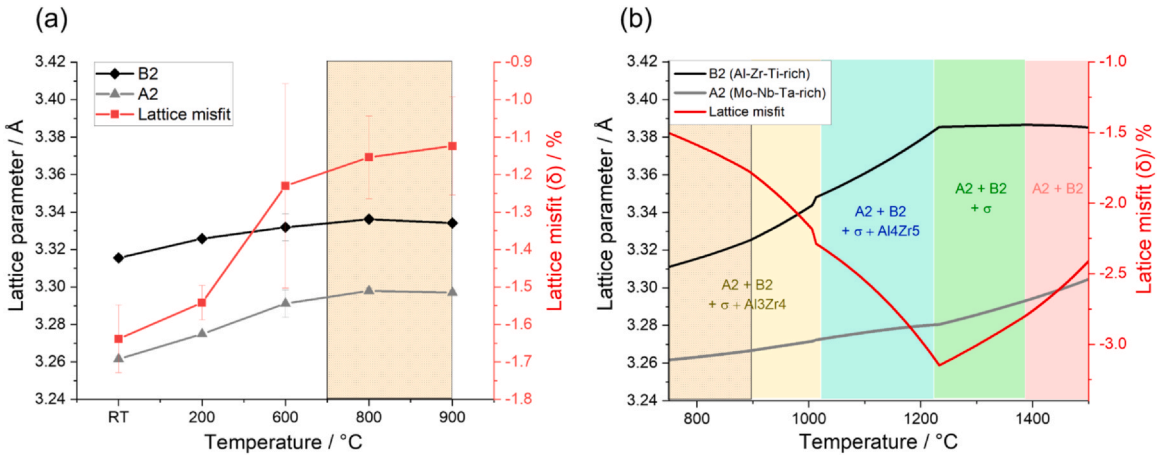

Fig. 6. Lattice parameters (left axis), and lattice misfit (right axis) of the A2 and B2 phases as a function of temperature. (a) Experimentally measured using *in-situ* XRD and (b) calculated using ThermoCalc (TCHEA3 database, version 2020b).

coherently embedded cuboids with edge lengths aligned along the elastically soft ‹100› directions to minimize the elastic strain energy [11,45]. In our case, for a slow cooling rate, the structure dwells longer at higher temperatures, where the wavelength of the fastest growing concentration waves from the spinodal decomposition is longer [58] and thus the size scale of the final A2 and B2 microstructure is coarser. Hence, a slow cooling rate leads to the formation of a low number density of large A2 precipitates, as also observed in spinodally decomposed Fe-Cr alloys with a high Cr content (*e.g.*, 40 wt% Cr)) [59].

Our TEM investigations in Fig. 2 show the presence of wide and narrow B2 channels as well as cubic and plate- shaped A2 precipitates in the $AlMo_{0.5}NbTa_{0.5}TiZr$ RSA. These features were already described by Senkov et al. [10], who reported that the large matrix channels are much more depleted in refractory elements than the narrow channels and the authors suggested that the former are too depleted in refractory elements to form the A2 precipitates. They argued that the spinodal decomposition takes place in two stages at different temperatures upon cooling: the high-temperature stage is responsible for the formation of refractory depleted wide B2 channels; during the second, low-temperature stage, thin B2 channels with higher amounts of refractory elements form. Thus, their reasoning is thermodynamic in nature [10]. Another explanation was proposed by Jensen [45] according to whom the formation of thin plate-shaped and cubic A2 precipitates in the RSA can be attributed to overlapping compositional waves on two orthogonal ‹100› directions. His assumption is that the superposition of two orthogonal wave maxima leads to the precipitation of A2 cubes and that of two orthogonal wave minima leads to large, squared regions of the B2 phase (*e.g.*, see red dashed framed regions in Fig. 2d). When a wave maximum overlaps with a minimum of an orthogonal wave, it leads to the formation of thin A2 plates separated by thin B2 channels. This process thus yields a mixture of cuboidal and platelet precipitates, as well as wide regions in between, especially for slow cooling rates. However, the latter mechanism proposed by Jensen seems incomplete. Overlaps between orthogonal waves, as such, do not have fast-changing compositional variations allowing phase separation. Instead, an additional step such as that proposed by Senkov et al. [10] at these locations would be required to rapidly reach the thermal equilibrium compositions that then allow the precipitation of thin A2 platelets separated by thin B2 channels. This step may happen simultaneously with the precipitation of the main overlapping maxima and not necessarily at low temperatures. Additional mechanisms may also play a role in shaping the microstructure of the RSA, as discussed in the following.

The three schematic drawings in Fig. 7, which were adapted from the work of Wang et al. [46], illustrate the microstructural evolution upon coarsening of a spinodally decomposed alloy with a lattice misfit between the two phases, which was described by Wang et al. [46], in the following manner: At the beginning of coarsening (Fig. 7a), the microstructure consists of a periodic array of aligned cubic precipitates with some defects. In our case this array could be found in the two incomplete rows of precipitates, highlighted by red dashed frames in Fig. 7a (described by Wang et al.) and Fig. 2 f (our experimental findings). This array is reminiscent of the extra half planes of atoms associated with an edge dislocation. Thus, at the end of these rows, there is a “macrodislocation” (according to Wang et al.) in reference to its resemblance to pure edge dislocations observed edge-on at atomic resolution. As a result of coarsening, the simulations by Wang et al. showed that the extra rows of precipitates are less stable and dissolve following a process similar to dislocation climb, leading to the coarsening of the A2 precipitates as well as the B2 channel width, which were also observed in our experiment (see dashed red rectangles in Figs. 7b,c and 2 d).

Additionally, the red and green arrows in Fig. 2d-f mark doublets of parallel A2 plates and presumably octets of A2 cubes (which we cannot capture in our 2D images), respectively, that presumably formed by the splitting of initially large cuboidal precipitates (note that the splitting is often asymmetric). These results can be rationalized based on the 2D simulations of spinodal decomposition in cubic alloys reported by Wang et. al. [46], who showed that when the elastic energy contribution dominates significantly over the interfacial energy contribution, the fastest way to relax the starting non-equilibrium shape to an equilibrium one of a precipitate could be *via* splitting.

Therefore, we think that the heterogeneous microstructure with wide and narrow B2 channels as well as cubic and plate-shaped A2 precipitates could result from the dynamic processes, described by Wang et. al. [46], associated with the complex coarsening behavior of the A2/B2 microstructure that is strongly affected by the lattice misfit between the A2/B2 phases as a function of time and temperature. The A2 platelets may either form through the mechanism proposed by Wang et al. [46], the mechanism proposed by Jensen [45], or a combination of the two. It may not, however, be ruled out that the mechanism of formation of the bimodal channel width simultaneously occurs by multiple times of

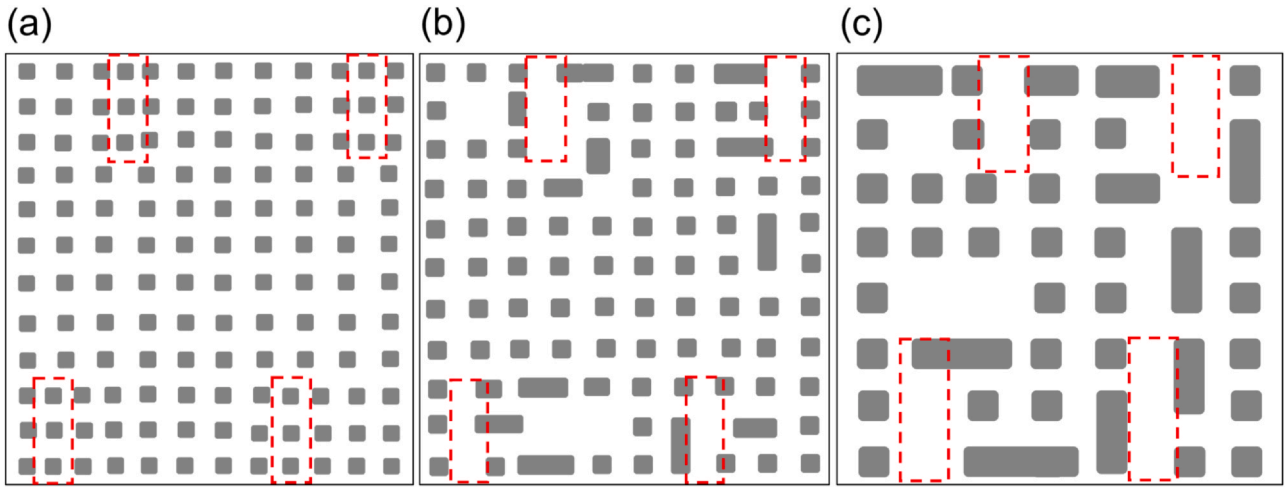

Fig. 7. Morphological evolutions upon coarsening in alloys undergoing an asymmetrical spinodal decomposition under a high strain energy (coherent lattice misfit) as described by Wang et al., [46], (a) beginning of the process (b) middle and (c) end of coarsening. The sketch was adapted from Figures 3b3-d3 in Ref [46].

Table 6
Vickers microhardness of the $AlMo_{0.5}NbTa_{0.5}TiZr$ RSA after different cooling rates for different applied loads ranging from 1 to 30 kg. At least 19 indentation tests were performed for each condition. The proportion (*Fc*) of cracks that developed at the corners of the indenter at a given load is indicated, *e.g.*, Fc_{HV30} = 76/80 means that among the 80 corners of the 20 remnant indents, 76 exhibited cracks. The uncertainties are given by the standard deviations.

State	Cooling rate (°C/min)	Hardness (HV1)	Hardness (HV20)	Hardness (HV30)	Fc_{HV20}	Fc_{HV30}
Annealing + HIP	5	629 ± 18	606 ± 12	592 ± 8	51/76	76/80
	10	644 ± 6	623 ± 10	609 ± 11	48/76	66/80
	30	667 ± 11	652 ± 10	634 ± 11	22/76	56/80

spinodal decomposition at different temperatures during cooling as proposed by Senkov et al. [7]. More experimental evidence is required to confirm this mechanism.

3.5. Influences of cooling rate and microstructure on room temperature strength

Indentation methods were employed to assess different aspects of the mechanical behavior of the RSA at different length scales. Microhardness tests with weights up to 30 kg were performed to estimate the strength of the alloy and fracture toughness averaged over several grains. Nanoindentation tests were carried out to evaluate the strength of the $A_{4-x}Zr_5$ hexagonal intermetallic at the grain boundaries, the strength of the A2/B2 microstructure within grains, and their contributions to the microhardness of the alloy. Table 6 summarizes the microhardness values of the RSA for different applied loads and different cooling rates. As expected, the microhardness of a given sample slightly decreases by ≈ 6 % with increasing applied load from 9.8 to 294 N. This size effect arises from the fact that, as the indented volume increases with increasing applied load, the probability of finding crystalline defects or pre-existing cracks in the indented volume increases, resulting in a lower hardness. The cooling rate is found to have a similar effect on strength, *i.e.*, the microhardness increases by 6–8 %, regardless of the applied load when the cooling rate increases from 5° to 30°C/min.

Nanoindentation tests were performed with a maximum applied load of 8 μN to evaluate the nanohardness of the hexagonal Al-Zr-rich intermetallic phase, and the A2/B2 regions for different cooling rates, *cf.* Table 7 and Fig. 8a. The nanohardness of the Al-Zr-rich intermetallic compound is ≈ 60 % larger than that of the A2/B2 nanostructure (Fig. 8a), *i.e.*, ≈ 13 GPa and ≈ 8 GPa for the Al-Zr-rich phase and A2/B2 regions, respectively, for a cooling rate of 30 °C/min. The nanohardness of the Al-Zr-rich intermetallic is approximately independent of the cooling rate because the morphology and composition of this hexagonal phase do not change with increasing cooling rate (see Fig. 1 and Table S2). In contrast, the nanohardness of the A2/B2 regions increases by ≈ 10 % when the cooling rate increases from 5° to 30°C/min, which is consistent with the microhardness results. However, it is worth noting that, owing to the low applied load, the nanohardness of the A2/B2 regions is not affected by grain boundaries, the Al-Zr-rich intermetallic phase, nor pre-existing cracks, contrary to the microhardness data. This is probably the reason for the smaller effect of cooling rate on microhardness (≈ 6 %) compared to that on nanohardness (≈ 10 %). As the cooling rate decreases, the strength of the A2/B2 regions decreases but this effect is mitigated by the increase in volume fraction of the hard Al-Zr-rich precipitates present at the grain boundaries.

To correlate the variation of strength with microstructural changes, we show in Fig. 8b how nanohardness depends on the mean edge length (d) of the A2 precipitates. Here, the nanohardness decreases from 8.8 GPa to 8.0 GPa while d increases from 16 to 25 nm, respectively. This size-dependence of the nanohardness (H) can be well described by the following empirical relationship: $\log H = \log H_0 + s \log d$, where H_0 is a constant (≈ 15.8 GPa) and s (≈ −0.2) is the slope of the log *H-versus*-log *d*-curve obtained by regression fitting of the data. It is expected that the parameters contributing to the nanohardness of the A2/B2 regions are related to the precipitate and channel sizes, the compositions of the A2 and B2 phases and the associated coherency stresses.

In the field of Ni- and Co-based superalloys, if the volume fraction of γ' phase remains constant, studies show that the size of the γ' precipitates becomes smaller by increasing the cooling rate. This results in an increase in hardness, which varies inversely with the size of the γ' precipitates [30,31]. This evolution can be attributed to an increase in dislocation density within the γ channels due to the disruption of dislocation motion by obstacles (precipitates) [31]. Since the RSA has a similar two-phase nanostructure with a cube-on-cube orientation relationship, the behavior of the bcc-structured RSA may be analogous to that of fcc-structured superalloys. However, the main difference is that, in the RSA, the matrix consists of a strong and ordered intermetallic reinforced by isolated cuboidal precipitates of a softer and disordered phase while in fcc-structured superalloys, the soft disordered matrix is reinforced by stronger ordered precipitates. Consequently, in the $AlMo_{0.5}NbTa_{0.5}TiZr$ RSA, dislocations must nucleate in the A2 precipitates while the B2 phase is still deformed elastically, resulting in a load transfer to the stronger B2 phase. The dislocations probably glide within A2 precipitates until they are stopped at the A2/B2 interfaces where they relax the lattice misfit. Based on this scenario, there are three main contributions to the strength of the alloy: the intrinsic properties of the individual phases, the coherency stresses and an Orowan contribution ($\tau_{Orowan} = \mu b/d$, where μ is the shear modulus, b the magnitude of the Burgers vector, and d is assumed as the narrowest average width within the A2 precipitates contained in the dislocation glide plane [60]). Of these three contributions, only the Orowan stress is microstructure-dependent and may be invoked to rationalize the evolution of nanohardness with the A2 size in Fig. 8b.

From the load-displacement curves obtained by nanoindentation (Fig. S9), we also determined the indentation moduli of the Al-Zr-rich intermetallic and the A2/B2 regions, see Table 7. Since the A2 precipitates and B2 channels are nanoscale (16–25 nm and 3–45 nm,

Table 7
Nanohardness, indentation modulus (E_r), and elastic modulus (E) calculated assuming a Poisson's ratio of 0.3 for each phase of the RSA after different cooling rates.

Cooling rate (°C/min)	Nanohardness (GPa)		E_r (GPa)		E (GPa)	
	Al-Zr-rich phase	A2/B2	Al-Zr-rich Phase	A2/B2	Al-Zr-rich phase	A2/B2
5	13.1 ± 0.5	8.0 ± 0.4	137 ± 8	112 ± 5	142 ± 8	113 ± 5
10	13.2 ± 0.5	8.5 ± 0.8	155 ± 10	121 ± 6	163 ± 10	123 ± 6
30	13.3 ± 0.7	8.8 ± 0.6	151 ± 9	115 ± 5	159 ± 9	116 ± 5

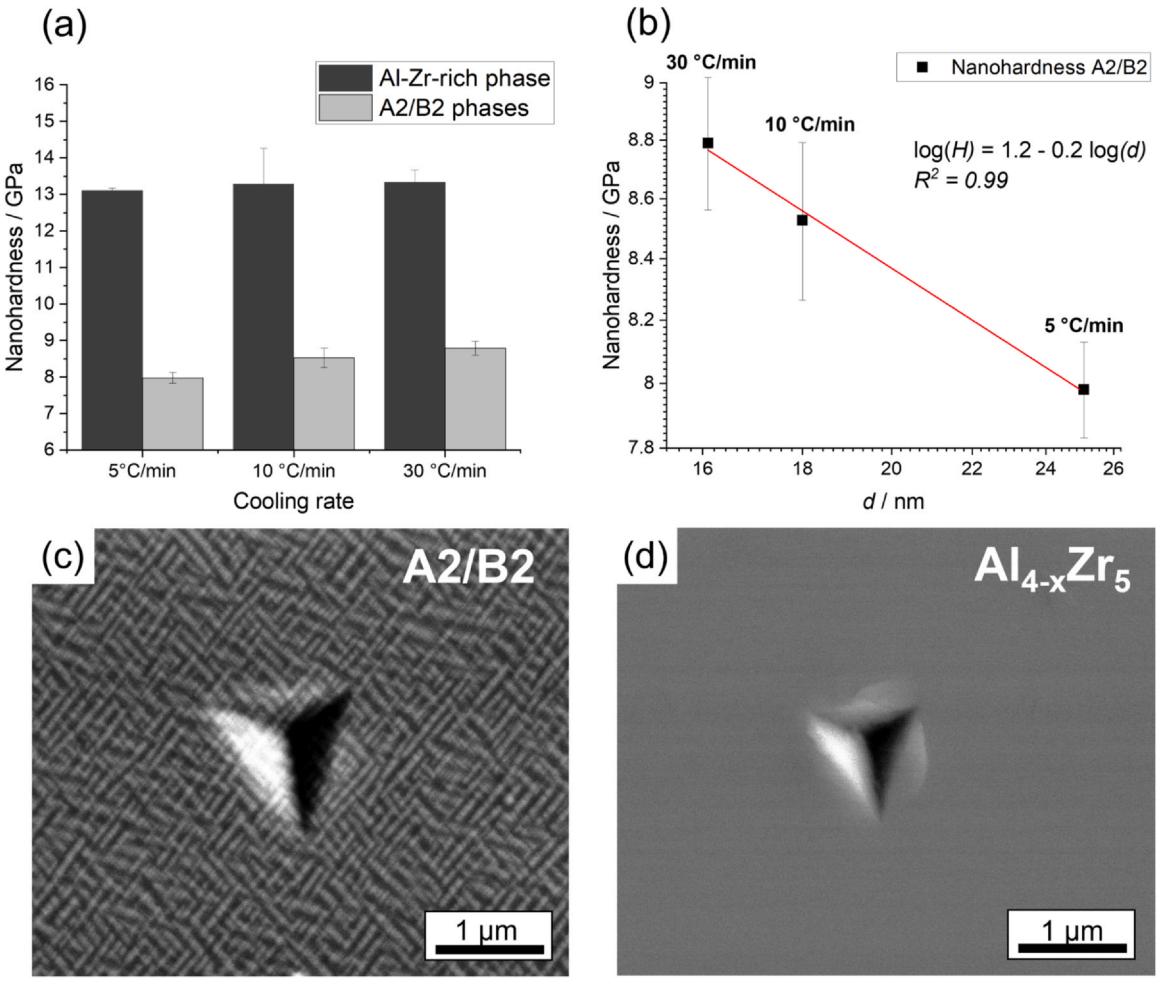

Fig. 8. (a) Nanohardness *vs.* cooling rate of different regions: within the A2/B2 substructure and the Al-Zr-rich phase, for the samples cooled at 5, 10, and 30 °C/min. (b) Nanohardness of the A2/B2 phase substructure *vs.* A2 precipitate mean size *d*. The red line in (b) represents the regression line obtained from the data. The error bars are given by the standard deviation. Representative BSE micrographs of remnant indents in the A2/B2 microstructure and the Al-Zr-rich phase are shown in (c) and (d), respectively.

respectively, see Table 2), their elastic moduli and hardness could not be measured separately by nanoindentation. Given experimental uncertainties, the indentation and Young's moduli are nearly independent of the cooling rate. The Al-Zr-rich intermetallics are ≈ 25 % stiffer than the A2/B2 regions. Assuming a Poisson's ratio of 0.3, the Young's modulus of the A2/B2 regions, which constitute at least 93 vol% of the alloy depending on the cooling rate, is 120 ± 5 GPa, consistent with the value reported by Senkov et al. [24] (122 GPa), which was obtained from compression tests.

3.6. Effect of cooling rate on fracture toughness

The fracture toughness (K_c) was estimated from the length and morphology of the cracks that formed at the corners of the micro-indenter tip. While no cracks were found after microindentation with an applied weight of 1 kg, cracks were clearly visible with higher weights of 20 and 30 kg. To estimate the fracture toughness, it is first necessary to determine the nature of the cracks. For this purpose, the ratios c/h and l/h were determined, where h is the length between the center and the corner of a remnant imprint, c is the crack length from the center of the indent to the crack tip, and l is the length between the corner of the indent and the tip of the crack, as exemplarily shown in Fig. 9. According to Niihara et al. and

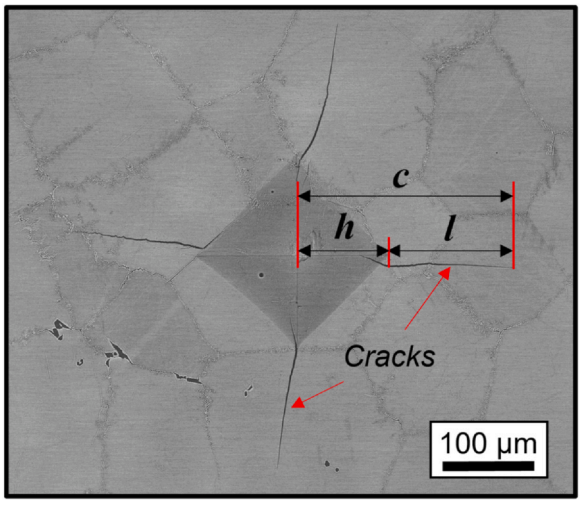

Fig. 9. BSE micrograph of a representative remaining Vickers indent with cracks emanating from all four corners, where h is the length of the half-diagonal of the indent and l is the crack length from the corner of the indent to the crack tip. The microhardness test was performed with a weight of 20 kg using an RSA cooled at 10 °C/min.

Table 8
Microhardness, crack length (l), indent diagonal (h), l/h ratio, and fracture toughness (K_c) of the RSA for the three studied cooling rates at different loads. Also shown in this table are elastic moduli determined by nanoindentation.

Cooling rate	F (N)	Hardness (GPa)	E (GPa)	h (μm)	c (μm)	l (μm)	l/h	K_c (MPa·m$^{1/2}$) [a]	K_c (MPa·m$^{1/2}$) [b]
5 °C/min	294.0	5.8 ± 0.1	115.3 ± 3.3	148.2 ± 0.6	309.6 ± 35.4	171.8 ± 36.5	1.2 ± 0.2	4.6 ± 0.5	4.6 ± 0.5
	196.0	5.9 ± 0.1		119.7 ± 1.1	264.7 ± 41.4	157.9 ± 40.2	1.3 ± 0.3	4.0 ± 0.5	3.9 ± 0.5
10 °C/min	294.0	6.0 ± 0.1	123.9 ± 3.4	144.0 ± 2.0	342.2 ± 54.4	212.4 ± 48.8	1.5 ± 0.3	4.5 ± 0.5	4.4 ± 0.5
	196.0	6.1 ± 0.1		116.0 ± 1.0	273.8 ± 29.7	168.7 ± 26.8	1.5 ± 0.3	3.8 ± 0.5	3.9 ± 0.4
30 °C/min	294.0	6.2 ± 0.1	116.2 ± 2.6	141.9 ± 1.3	348.1 ± 46.4	221.9 ± 40.8	1.6 ± 0.3	-	4.2 ± 0.4
	196.0	6.4 ± 0.1		115.9 ± 0.6	278.2 ± 20.1	175.6 ± 22.4	1.5 ± 0.2	-	3.8 ± 0.3

[a] considering only the indentations for which four primary cracks emanated straight and radially from each corner. When no value is provided, it means that there were no indentations with four primary cracks.
[b] considering all indentations that contained at least one crack emanating from a corner.

Schiffmann [39,61], the cracks either have a half-penny shape that joins the tips of two cracks located on opposite sides of the indent when $c/h \geq 2.5$ (the total length of a half-penny crack projected on the sample surface corresponds to $2c$) or they are of Palmqvist type when $0.25 \leq l/h \leq 2.5$, *i.e.*, they are much shorter and form circular arcs right below the visible cracks (projected length of each crack: l).

In this study, since $0.25 \leq l/h \leq 2.5$ in the $AlMo_{0.5}NbTa_{0.5}TiZr$ RSA, the cracks are of Palmqvist type and the fracture toughness K_c, also known as indentation fracture resistance [62] can be calculated using:

$$K_c = A\left(\frac{E}{H}\right)^{2/5}\frac{P}{hl^{1/2}} \quad (5)$$

where factor A is a constant equal to 0.009. E is the elastic modulus obtained from the nanoindentation tests, H is the measured microhardness, and P is the indentation load. The parameters in Eq. 5 required to compute K_c are listed in Table 8 for the samples cooled at different rates. The fracture toughness (K_c) of the RSA was calculated using two different criteria. In the first case [a], we only considered at least five remnant indents with cracks emanating from each corner following the standard test method ISO 21618 [40], see K_c [a] in Table 8. In the second case [b], all the indents (10–15 independent measurements) that showed at least one crack were considered to estimate K_c [b]. Given the experimental errors, the average K_c value of 4.2 ± 0.4 is not significantly affected by criteria [a] and [b], the applied load, and cooling rate, see Table 8.

Additionally, we estimated in Table 6 another parameter that is related to the fracture toughness, *i.e.*, the fraction of cracks (F_c) observed at the corners of the remnant microindents as described in Section 2.2. The fraction of cracks is found to increase with increasing applied load for a given cooling rate. We believe that this is related to a sampling effect, *i.e.*, the larger the applied load, the greater the indented volume, and the higher the likelihood to nucleate a crack at a defect. F_c decreases with increasing cooling rate. There may be two microstructural features that contribute to this phenomenon. First, as the cooling rate increases, the precipitation of the brittle Al-Zr-rich intermetallic at grain boundaries is progressively suppressed. Second, as the size of the A2 precipitates decreases at an increased cooling rate, the density of A2/B2 interfaces, which may impede crack nucleation and propagation, increases.

With all this new data, the alloy can now be compared to other material classes. The Ashby plot displayed in Fig. 10 shows the fracture toughness as a function of Vickers microhardness for different groups of engineering materials. These groups, marked with gray areas, include foams, elastomers, polymers, composites, technical and non-technical ceramics, glasses, and engineering alloys as well as other bcc-structured alloys that are highlighted in color. For

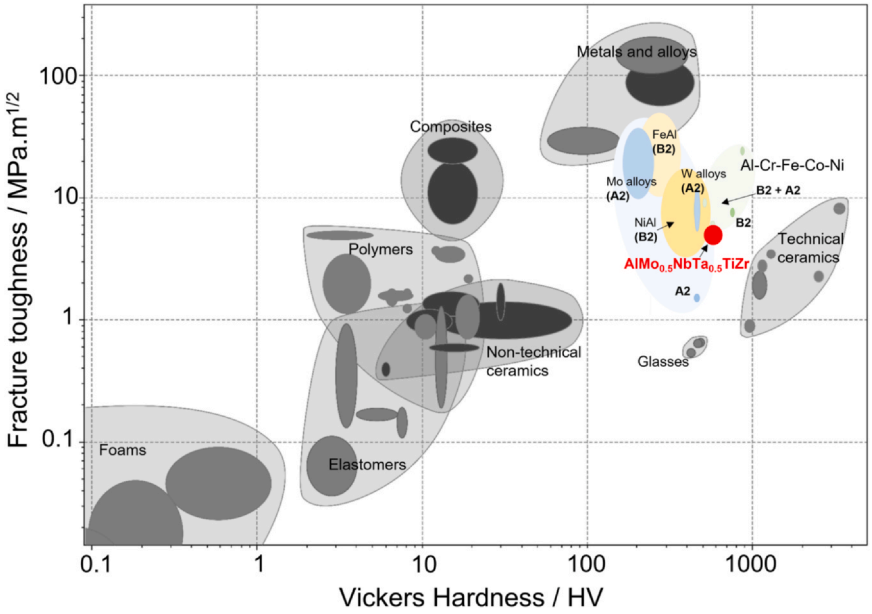

Fig. 10. Ashby plot, obtained with the Granta Edupack software, of different engineering materials showing their fracture toughness *vs.* Vickers microhardness. The red area highlights the $AlMo_{0.5}NbTa_{0.5}TiZr$ RSA investigated in the present study. The other colored regions correspond to other bcc-structured alloys.

Table 9
Mechanical properties at RT (Vickers hardness and fracture toughness) of different alloys and intermetallics with bcc structures reported in the literature.

Alloys	Structure	Hardness (HV)	Fracture toughness ($MPa{\cdot}m^{1/2}$)	Method	Reference
NiAl	B2	330 [63]	5.08 – 6.42	Vickers indentation (ring on ring disk bend test)	[65]
NiAl	B2	460–560 (4.5–5.5 GPa) [64]	10.6 – 14.8	Fatigue tests of pre-cracked specimens following the ASTM E399 standard	[66]
NiAl	B2		13.0 – 17.0	Double cantilever beam	[67]
Ni-50Al	B2		3.79 – 9.31	Fatigue tests of pre-cracked specimens following the ASTM E399 standard	[68]
Ni-46Al			3.00 – 3.09		
Fe40Al	B2 + A2 Fe (Al)	867	23.8	Vickers indentation	[69]
Co-40Al	B2		2.20	Fatigue tests of pre-cracked specimens following the ASTM E399 standard	[68]
Co-49Al			3.08		
Fe-40Al	B2	197–380 [70]	33.3 – 55.8		[68]
Fe-48Al			11.7		
W and some W-alloy	A2	367–389 [71]	5.4 – 13.5		[72]
Molybdenum-base alloys					
TZM-Mo	A2	230–262 [73]	10.0 – 27.5		[74]
ODS-Mo			27.8 –147.32		
LCAC			14.6 – 38.5		
$Al_{23}Co_{15}Cr_{23}Cu_8Fe_{15}Ni_{15}$	A2 + B2 + fcc	545 (5.3 GPa)	5.8	Pre-cracked ASTM E399	[67]
			5.4	Chevron notched rectangular bar (CVNRB)	
$Al_{18}Cr_{21}Fe_{20}Co_{20}Ni_{21}$	A2 + B2 + fcc	508	9.0	Pre-cracked ASTM E399	[75]
$FeCoNiCrAl_3$	B2	740	7.6	Vickers indentation	[76]
$Nb_{25}Mo_{25}Ta_{25}W_{25}$	A2	455 (4.46 GPa) [77]	1.6	Bending of notched micro-cantilever	[78]
HfNbTaTiZr	A2	509 [79]	210	Single specimen compliance method for *J*-integral measurement (ASTM E1820–17 standard)	[80]
AlCuTaVW	two fcc + B2	1326 (13 GPa)	8.36	Vickers indentation	[81]

instance, the toughness/hardness combination of the Al-$Mo_{0.5}NbTa_{0.5}TiZr$ RSA (red dot in Fig. 10, present work) is compared to those of B2 intermetallics (NiAl and FeAl, orange areas), single-phase A2 metals and alloys (blue regions), and two-phase A2/B2 compositionally complex alloys from the Al-Cr-Fe-Co-Ni system (green) and the corresponding data is summarized in Table 9 As shown in Fig. 10, the fracture toughness and Vickers hardness of the RSA are intermediate between those of technical ceramics and engineering alloys. However, its toughness/hardness combination is similar to those of B2 intermetallics and two-phase A2/B2 alloys.

4. Conclusion and summary

In the present work, the effects of the cooling rate on microstructure, hardness, and fracture toughness of $AlMo_{0.5}NbTa_{0.5}TiZr$ RSA were investigated. From our results, it can be concluded that increasing the cooling rate produces a finer and more homogeneous A2/B2 substructure and suppresses grain boundary precipitation of the hexagonal $Al_{4-x}Zr_5$ intermetallic phase, which improves the hardness of the alloy but does not reduce its brittleness. Some of the key findings can be summarized as follows:

1. The volume fraction of the hexagonal $Al_{4-x}Zr_5$ intermetallic compound can be reduced to < 1 % with a cooling rate of at least 30 °C/min. In contrast, the relative volume fractions of the A2 and B2 phases remain approximately unaffected by the cooling rate. The nanohardnesses of the $Al_{4-x}Zr_5$ intermetallic and A2/B2 regions are ≈ 13 and 8–9 GPa, respectively.
2. The cooling rate affects the size, aspect ratio, and size distribution of the A2 cuboidal precipitates. When the cooling rate increases from 5° to 30°C/min, the size of the A2 precipitates decreases from 25 to 16 nm, resulting in an increase in microhardness of ≈ 6 % (averaged over different phases and grains). In addition, a high cooling rate promotes the formation of more cubic precipitates while they are elongated and form slabs at lower cooling rates. The cooling rate does not affect the composition of the A2 and B2 phases.
3. While the lattice parameter of the hexagonal Al-Zr-rich phase is unaffected by the cooling rate, those of the A2 and B2 phases become more similar with an increasing cooling rate, thus resulting in a decrease of the constrained lattice misfit.
4. With increasing temperature, the lattice parameter of the A2 phase expands at a higher rate than that of the B2 phase, owing to a higher coefficient of thermal expansion of the former, thus resulting in a decrease of the lattice misfit, which becomes less negative.
5. The fracture toughness $K_c = 4.2 \pm 0.4\ MPa{\cdot}m^{1/2}$ of the RSA is independent of the cooling rate and its value is comparable to that of most B2 intermetallics and two-phase A2/B2 alloys reported in the literature. From a general viewpoint, the fracture toughness of the RSA lies between that of engineering alloys and ceramics.

While this paper focuses on the room temperature properties of the RSA, it is important to note that the tensile properties at high temperatures are also critical for its potential use in structural applications. Therefore, results of tensile creep tests will be presented in a subsequent contribution, which will provide a more complete picture of the suitability of the alloy for high-temperature applications.

CRediT authorship contribution statement

Patricia Suárez Ocano: Experimental methodology, Formal analysis, Data curation, Writing – original draft. **Anna Manzoni:** XRD and *in-situ* XRD analysis, Methodology, Writing – review & editing. **Inmaculada Lopez-Galilea** and **Benjamin Ruttert:** Methodology (HIP treatment), Writing – review & editing. **Guillaume Laplanche:** Conceptualization, Methodology, Writing – review & editing, Supervision. **Leonardo Agudo Jácome:** Conceptualization,

Methodology, TEM measurements, Formal analysis, Writing – review & editing, Supervision and Funding acquisition.

Data availability

Data will be made available on request.

Declaration of Competing Interest

The authors declare that they have no known competing financial interests or personal relationships that could have appeared to influence the work reported in this paper.

Acknowledgements

PSO, LAJ and GL acknowledge funding through projects n°. 398838389 and LA/3607-2, respectively, from the Deutsche Forschungsgemeinschaft (DFG). ILG acknowledge the DFG for the funding through project No. 503229465 and the Collaborative Research Center SFB/TR 103 (Project T4). The authors thank Stephan Laube, Dr. Alexander Kaufmann, Prof. Martin Heilmaier, at KIT for the fabrication of the alloy as well as Prof. Theisen at RUB for HIP treatment. The authors acknowledge Steffen Thärig, Christine Krimmling, and Dr. Birgit Rehmer, and Oliver Schwarze at BAM for assistance with the microhardness and nanoindentation tests, respectively. The authors acknowledge R. Schwiddessen and M. Tovar for helping in performing the *in-situ* X-ray diffraction experiments and the HZB X-ray Core Lab. Parts of this work were performed at the electron microscopy center at BAM. PSO acknowledge Suzana G. Fries at RUB and Huahai Mao at Thermocalc for valuable opinions about the CALPHAD analysis. The authors acknowledge Prof. Yunzhi Wang for the fruitful discussion on the microstructural mechanisms.

Appendix A. Supporting information

Supplementary data associated with this article can be found in the online version at doi:10.1016/j.jallcom.2023.169871.

References

[1] B.Q. Chen, L.C. Zhuo, Latest progress on refractory high entropy alloys: composition, fabrication, post processing, performance, simulation and prospect, Int. J. Refract Met Hard Mater. 110 (2023), https://doi.org/10.1016/j.ijrmhm.2022.105993

[2] S.K. Dewangan, A. Mangish, S. Kumar, A. Sharma, B. Ahn, V. Kumar, A review on high-temperature applicability: a milestone for high entropy alloys, Eng. Sci. Technol. 35 (2022), https://doi.org/10.1016/j.jestch.2022.101211

[3] S. Naka, Development of intermetallic materials for structural applications: toward designing multi-constituent and/or multi-phase alloys, J. Phys. IV 6 (C2) (1996) 147–152, https://doi.org/10.1051/jp4:1996220

[4] M. Wang, Z.L. Ma, Z.Q. Xu, X.W. Cheng, Designing VxNbMoTa refractory high-entropy alloys with improved properties for high-temperature applications, Scr. Mater. 191 (2021) 131–136, https://doi.org/10.1016/j.scriptamat.2020.09.027

[5] W.J. Huang, X.J. Wang, J.W. Qiao, Y.C. Wu, Microstructures and mechanical properties of TiZrHfNbTaWx refractory high entropy alloys, J. Alloy Compd. 914 (2022), https://doi.org/10.1016/j.jallcom.2022.165187

[6] H.J. Zhang, Y.H. Du, L.M. Lai, N. Guo, N. Li, S.F. Guo, The as-cast Al_xCrTaTi refractory medium entropy alloys with good room-temperature mechanical properties and high-temperature oxidation resistance, J. Alloy Compd. 932 (2023), https://doi.org/10.1016/j.jallcom.2022.167675

[7] D.B. Miracle, M.H. Tsai, O.N. Senkov, V. Soni, R. Banerjee, Refractory high entropy superalloys (RSAs, Scr. Mater. 187 (2020) 445–452, https://doi.org/10.1016/j.scriptamat.2020.06.048

[8] O.N. Senkov, S. Gorsse, D.B. Miracle, High temperature strength of refractory complex concentrated alloys, Acta Mater. 175 (2019) 394–405, https://doi.org/10.1016/j.actamat.2019.06.032

[9] J. Startt, A. Kustas, J. Pegues, P. Yang, R. Dingreville, Compositional effects on the mechanical and thermal properties of MoNbTaTi refractory complex concentrated alloys, Mater. Des. 213 (2022), https://doi.org/10.1016/j.matdes.2021.110311

[10] O. Senkov, D. Isheim, D. Seidman, A. Pilchak, Development of a refractory high entropy superalloy, Entropy 18 (3) (2016) 102, https://doi.org/10.3390/e18030102

[11] J.K. Jensen, B.A. Welk, R.E.A. Williams, J.M. Sosa, D.E. Huber, O.N. Senkov, G.B. Viswanathan, H.L. Fraser, Characterization of the microstructure of the compositionally complex alloy $Al_1Mo_{0.5}Nb_1Ta_{0.5}Ti_1Zr_1$, Scr. Mater. 121 (2016) 1–4, https://doi.org/10.1016/j.scriptamat.2016.04.017

[12] T.E. Whitfield, H.J. Stone, C.N. Jones, N.G. Jones, Microstructural degradation of the $AlMo_{0.5}NbTa_{0.5}TiZr$ refractory metal high-entropy superalloy at elevated temperatures, Entropy 23 (1) (2021) 80, https://doi.org/10.3390/e23010080

[13] P. Suárez Ocaño, S.G. Fries, I. Lopez-Galilea, R.D. Kamachali, J. Roik, L. Agudo Jácome, The $AlMo_{0.5}NbTa_{0.5}TiZr$ refractory high entropy superalloy: experimental findings and comparison with calculations using the CALPHAD method, Mater. Des. 217 (2022) 110593, https://doi.org/10.1016/j.matdes.2022.110593

[14] Z.T. Kloenne, J.-P. Couzinié, M. Heczko, R. Gröger, G.B. Viswanathan, W.A.T. Clark, H.L. Fraser, On the bcc/B2 interface structure in a refractory high entropy alloy, Scr. Mater. 223 (2023) 115071, https://doi.org/10.1016/j.scriptamat.2022.115071

[15] M.J. Mehl, D. Hicks, C. Toher, O. Levy, R.M. Hanson, G. Hart, S. Curtarolo, The AFLOW library of crystallographic prototypes: part 1, Comp. Mater. Sci. 136 (2017) S1–S828, https://doi.org/10.1016/j.commatsci.2017.01.017

[16] L.A. Morales, N. Luo, K. Li, C.H. Zenk, C. Korner, On stabilizing an $\alpha/\alpha'/\alpha''$ microstructure in ferritic superalloys, J. Alloy. Compd. 911 (2022) 164996, https://doi.org/10.1016/j.jallcom.2022.164996

[17] R.C. Reed, K.A. Green, P. Caron, T.P. Gabb, M.G. Fahrmann, E.S. Huron, S.A. Woodard, Superalloys 2008, TMS, Warrendale PA, 2008. doi: 10.1017/S0001924000087509.

[18] J.L. Li, Z. Li, Q. Wang, C. Dong, P.K. Liaw, Phase-field simulation of coherent BCC/B2 microstructures in high entropy alloys, Acta Mater. 197 (2020) 10–19, https://doi.org/10.1016/j.actamat.2020.07.030

[19] N. Yurchenko, E. Panina, A. Tojibaev, V. Novikov, G. Salishchev, S. Zherebtsov, N. Stepanov, Effect of B2 ordering on the tensile mechanical properties of refractory $Al_xNb_{40}Ti_{40}V_{20-x}$ medium-entropy alloys, J. Alloy Compd. 937 (2023), https://doi.org/10.1016/j.jallcom.2022.168465

[20] A. Asabre, P. Gemagami, A.B. Parsa, C. Wagner, A. Kostka, G. Laplanche, Influence of Mo/Cr ratio on the lamellar microstructure and mechanical properties of as-cast $Al_{0.75}$CoCrFeNi compositionally complex alloys, J. Alloy. Compd. 899 (2022) 163183, https://doi.org/10.1016/j.jallcom.2021.163183

[21] J.Y. Pang, H.W. Zhang, L. Zhang, Z.W. Zhu, H.M. Fu, H. Li, A.M. Wang, Z.K. Li, H.F. Zhang, Simultaneous enhancement of strength and ductility of body-centered cubic TiZrNb multi-principal element alloys via boron-doping, J. Mater. Sci. Technol. 78 (2021) 74–80, https://doi.org/10.1016/j.jmst.2020.10.043

[22] Y.G. Dong, S. Chen, N.N. Jia, Q.H. Zhang, L. Wang, Y.F. Xue, K. Jin, Microstructures and mechanical properties of Ta-Nb-Zr-Ti-Al refractory high entropy alloys with varying Ta/Ti ratios, Tungsten 3 (4) (2021) 406–414, https://doi.org/10.1007/s42864-021-00111-8

[23] T.E. Whitfield, G.J. Wise, H.J. Stone, N.G. Jones, The influence of the Nb:Ta ratio on the microstructural evolution in refractory metal superalloy systems, Appl. Phys. Lett. 119 (21) (2021), https://doi.org/10.1063/5.0068045

[24] O.N. Senkov, J.K. Jensen, A.L. Pilchak, D.B. Miracle, H.L. Fraser, Compositional variation effects on the microstructure and properties of a refractory high-entropy superalloy $AlMo_{0.5}NbTa_{0.5}TiZr$, Mater. Des. 139 (2018) 498–511, https://doi.org/10.1016/j.matdes.2017.11.033

[25] V. Soni, O.N. Senkov, B. Gwalani, D.B. Miracle, R. Banerjee, Microstructural design for improving ductility of an initially brittle refractory high entropy alloy, Sci. Rep. 8 (2018), https://doi.org/10.1038/s41598-018-27144-3

[26] X. Liu, K. Vecchio, Processing, microstructure evolution and mechanical property improvements of an Al-V-Cr-Mn-Fe-Ni CCA with an as-cast BCC/B2 coherent nanostructure, Mater. Sci. Eng. a Struct. 852 (2022), https://doi.org/10.1016/j.msea.2022.143698

[27] Z.J. Xu, Z.T. Li, Y. Tong, W.D. Zhang, Z.G. Wu, Microstructural and mechanical behavior of a $CoCrFeNiCu_4$ non-equiatomic high entropy alloy, J. Mater. Sci. Technol. 60 (2021) 35–43, https://doi.org/10.1016/j.jmst.2020.03.078

[28] M. Wischi, K.N. Campo, L.F. Starck, E.B. da Fonseca, S.N. Lopes, R. Caram, Microstructure and mechanical behavior of the directionally solidified $AlCoCrFeNi_{2.1}$ eutectic high-entropy alloy, J. Mater. Res Technol. 20 (2022) 811–820, https://doi.org/10.1016/j.jmrt.2022.07.065

[29] X. Wang, W. Zhai, J.Y. Wang, B. Wei, Strength and ductility enhancement of high-entropy $FeCoNi_2Al_{0.9}$ alloy by ultrasonically refining eutectic structures, Scr. Mater. 225 (2023), https://doi.org/10.1016/j.scriptamat.2022.115154

[30] M.A. Ali, I. López-Galilea, S. Gao, B. Ruttert, W. Amin, O. Shchyglo, A. Hartmaier, W. Theisen, I. Steinbach, Effect of γ' precipitate size on hardness and creep properties of Ni-base single crystal superalloys: experiment and simulation, Materialia 12 (2020) 100692, https://doi.org/10.1016/j.mtla.2020.100692

[31] H.R. Abedi, O.A. Ojo, X. Cao, Effect of cooling rate on precipitation behavior of gamma prime in a newly developed co-based superalloy, JOM 72 (2020) 4054–4059, https://doi.org/10.1007/s11837-020-04241-1

[32] H.L. Huang, Y. Sun, P.P. Cao, Y. Wu, X.J. Liu, S.H. Jiang, H. Wang, Z.P. Lu, On cooling rates dependence of microstructure and mechanical properties of refractory high-entropy alloys HfTaTiZr and HfNbTiZr, Scr. Mater. 211 (2022), https://doi.org/10.1016/j.scriptamat.2022.114506

[33] W. Lonski, M. Spilka, M. Kadziolka-Gawel, P. Gebara, A. Radon, T. Warski, K. Mlynarek-Zak, R. Babilas, The effect of cooling rate on the structure and selected properties of $AlCoCrFeNiSi_x$ (x=0; 0.25; 0.5; 0.75) high entropy alloys, J. Alloy Compd. 905 (2022), https://doi.org/10.1016/j.jallcom.2022.164074

[34] A. Munitz, S. Salhov, G. Guttmann, N. Derimow, M. Nahmany, Heat treatment influence on the microstructure and mechanical properties of $AlCrFeNiTi_{0.5}$ high entropy alloys, Mater. Sci. Eng. a Struct. 742 (2019) 1–14, https://doi.org/10.1016/j.msea.2018.10.114

[35] K. Xiong, L. Huang, X.F. Wang, L. Yu, W. Feng, Cooling-rate effect on microstructure and mechanical properties of $Al_{0.5}$CoCrFeNi high-entropy alloy, Metals 12 (8) (2022), https://doi.org/10.3390/met12081254

[36] A.C. Fischer-Cripps, Nanoindentation, Springer, New South Wales, Australia, 2011, https://doi.org/10.1007/978-1-4757-5943-3

[37] W.C. Oliver, G.M. Pharr, An improved technique for determining hardness and elastic-modulus using load and displacement sensing indentation experiments, J. Mater. Res. 7 (1992) 1564–1583, https://doi.org/10.1557/JMR.1992.1564

[38] Y.L. Shen, Handbook of mechanics of materials, in: S. Schmauder, C.S. Chen, K. Chawla, N. Chawla, W. Chen, Y. Kagawa (Eds.), Nanoindentation for Testing Material Properties, Springer, Singapore, 2019, pp. 1981–2012, https://doi.org/10.1007/978-981-10-6884-3_46

[39] K. Niihara, R. Morena, D.P.H. Hasselman, Evaluation of K_{Ic} of brittle solids by the indentation method with low crack-to-indent ratios, J. Mater. Sci. Lett. 1 (1) (1982) 13–16, https://doi.org/10.1007/Bf00724706

[40] Fine ceramics (advanced ceramics, advanced technical ceramics), Test Method for Fracture Resistance of Monolithic Ceramics at Room Temperature by Indentation Fracture (IF) Method, International Standard ISO 21618, 2019, 4–9.

[41] Standard Test Methods for Determining Average Grain Size, ASTM Designation: E112, 2013. doi:

[42] J. Schindelin, I. Arganda-Carreras, E. Frise, V. Kaynig, M. Longair, T. Pietzsch, S. Preibisch, C. Rueden, S. Saalfeld, B. Schmid, J.Y. Tinevez, D.J. White, V. Hartenstein, K. Eliceiri, P. Tomancak, A. Cardona, Fiji: an open-source platform for biological-image analysis, Nat. Methods 9 (7) (2012) 676–682, https://doi.org/10.1038/nmeth.2019

[43] W. Kraus, G. Nolze, POWDER CELL - a program for the representation and manipulation of crystal structures and calculation of the resulting X-ray powder patterns, J. Appl. Crystallogr. 29 (1996) 301–303, https://doi.org/10.1107/S0021889895014920

[44] H.L. Chen, H.H. Mao, Q. Chen, Database development and Calphad calculations for high entropy alloys: challenges, strategies, and tips, Mater. Chem. Phys. 210 (2018) 279–290, https://doi.org/10.1016/j.matchemphys.2017.07.082

[45] J.K. Jensen, Characterization of a high strength, refractory high entropy alloy, $AlMo_{0.5}NbTa_{0.5}TiZr$, Mater. Sci. Eng. Ohio State Univ. (2017) 227.

[46] Y. Wang, L.Q. Chen, A.G. Khachaturyan, Kinetics of strain-induced morphological transformation in cubic alloys with a miscibility gap, Acta Metall. Mater. 41 (1) (1993) 279–296, https://doi.org/10.1016/0956-7151(93)90359-Z

[47] K. Kadirvel, Z. Kloenne, J.K. Jensen, H. Fraser, Y.Z. Wang, Phase-field modelling of transformation pathways and microstructural evolution in multi-principal element alloys, Appl. Phys. Lett. 119 (17) (2021) 171905, https://doi.org/10.1063/5.0065522

[48] Y. Ma, B. Jiang, C. Li, Q. Wang, C.D. 1, P.K. Liaw, F. Xu, Lixian, The BCC/B2 morphologies in Al_xNiCoFeCr high-entropy alloys, Metals 7 (2017) 57, https://doi.org/10.3390/met7020057

[49] M. Akhlaghi, T. Steiner, S.R. Meka, E.J. Mittemeijera, Misfit-induced changes of lattice parameters in two phase systems: coherent/incoherent precipitates in a matrix, J. Appl. Crystallogr 49 (2016) 69–77, https://doi.org/10.1107/S1600576715022608

[50] H. Mughrabi, The importance of sign and magnitude of γ/γ' lattice misfit in superalloys-with special reference to the new γ'-hardened cobalt-base superalloys, Acta Mater. 81 (2014) 21–29, https://doi.org/10.1016/j.actamat.2014.08.005

[51] D.A. Porter, K.E. Easterling, M.Y. Sherif, Phase Transformations in Metals and Alloys, CRC Press, 2009.

[52] A.J. Goodfellow, L.R. Owen, K.A. Christofidou, J. Kelleher, M.C. Hardy, H.J. Stone, The effect of temperature and Mo content on the lattice misfit of model Ni-based superalloys, Metals 9 (6) (2019) 700, https://doi.org/10.3390/met9060700

[53] M.P. Jackson, R.C. Reed, Heat treatment of UDIMET 720Li: the effect of microstructure on properties, Mater. Sci. Eng. A 259 (1) (1999) 85–97, https://doi.org/10.1016/S0921-5093(98)00867-3

[54] M. Schwind, J. Kallqvist, J.O. Nilsson, J. Agren, H.O. Andren, σ-phase precipitation in stabilized austenitic stainless steels, Acta Mater. 48 (10) (2000) 2473–2481, https://doi.org/10.1016/S1359-6454(00)00069-0

[55] Y.S. Sato, H. Kokawa, Preferential precipitation site of sigma phase in duplex stainless steel weld metal, Scr. Mater. 40 (6) (1999) 659–663, https://doi.org/10.1016/S1359-6462(98)00483-7

[56] C.M.F. Rae, R.C. Reed, The precipitation of topologically close-packed phases in rhenium-containing superalloys, Acta Mater. 49 (19) (2001) 4113–4125, https://doi.org/10.1016/S1359-6454(01)00265-8

[57] F. Otto, A. Dlouhý, K.G. Pradeep, M. Kuběnová, D. Raabe, G. Eggeler, E.P. George, Decomposition of the single-phase high-entropy alloy CrMnFeCoNi after prolonged anneals at intermediate temperatures, Acta Mater. 112 (2016) 40–52, https://doi.org/10.1016/j.actamat.2016.04.005

[58] J.W. Cahn, J.E. Hilliard, Free energy of a nonuniform system. 1. Interfacial Free Energy, J. Chem. Phys. 28 (2) (1958) 258–267, https://doi.org/10.1063/1.1744102

[59] X. Xu, J. Odqvist, M.H. Colliander, S. King, M. Thuvander, A. Steuwer, P. Hedström, Effect of cooling rate after solution treatment on subsequent phase separation during aging of Fe-Cr alloys: a small-angle neutron scattering study, Acta Mater. 134 (2017) 221–229, https://doi.org/10.1016/j.actamat.2017.06.001

[60] G. Kostorz, H.A. Calderon, J.L. Martin, Fundamental Aspects of Dislocation Interactions: Low-Energy Dislocation Structures III, Mater. Sci. Eng. A Structural Materials Properties Microstructure and Processing Ascona, Switzerland, 1993. doi: 10.1016/C2013–0-12062–4.

[61] K.I. Schiffmann, Determination of fracture toughness of bulk materials and thin films by nanoindentation: comparison of different models, Philos. Mag. 91 (7–9) (2011) 1163–1178, https://doi.org/10.1080/14786435.2010.487984

[62] G.D. Quinn, Fracture toughness of ceramics by the vickers indentation crack length method: a critical review, Ceram. Eng. Sci. Proc. 27 (2) (2007) 45–62, https://doi.org/10.1002/9780470291313.ch5

[63] T. Haubold, R. Bohn, R. Birringer, H. Gleiter, Nanocrystalline intermetallic compounds—structure and mechanical properties, in: Proceedings of the Second International ASM Conference on High Temperature Aluminides and Intermetallics, High Temperature Aluminides and Intermetallics San Diego, CA, USA, 1992, 679–683.

[64] T. Chen, J.M. Hampikian, N.N. Thadhani, Synthesis and characterization of mechanically alloyed and shock-consolidated nanocrystalline NiAl intermetallic, Acta Mater. 47 (8) (1999) 2567–2579, https://doi.org/10.1016/S1359-6454(99)00059-2

[65] T. Kim, K.T. Hong, K.S. Lee, The relationship between the fracture toughness and grain boundary character distribution in polycrystalline NiAl, Intermetallics 11 (2003) 33–39, https://doi.org/10.1016/S0966-9795(02)00167-X

[66] J.W. Hoehn, S.K. Venkataraman, H. Huang, W.W. Gerberich, Micromechanical toughness test applied to NiAl, Mater. Sci. Eng. A 192 (1995) 301–308, https://doi.org/10.1016/0921-5093(94)03259-9

[67] U. Roy, H. Roy, H. Daoud, U. Glatzel, K.K. Ray, Fracture toughness and fracture micromechanism in a cast AlCoCrCuFeNi high entropy alloy system, Mater. Lett. 132 (2014) 186–189, https://doi.org/10.1016/j.matlet.2014.06.067

[68] K.M. Chang, R. Darolia, H.A. Lipsitt, Cleavage fracture in B2 aluminides, Acta Metall. Mater. 10 (1992) 2727–2737, https://doi.org/10.1016/0956-7151(92)90343-D

[69] X.T. Luo, C.J. Li, Dual-scale oxide dispersoids reinforcement of Fe-40 at%Al intermetallic coating for both high hardness and high fracture toughness, Mater. Sci. Eng. A 555 (2012) 85–92, https://doi.org/10.1016/j.msea.2012.06.037

[70] D. Siemiaszko, I. Garwacka, Unexpected high ductility of Fe40Al alloys at room temperature, Materials 14 (17) (2021) 4906, https://doi.org/10.3390/ma14174906

[71] Z.B. Li, H. Zhang, G.H. Zhang, K.C. Chou, Fabrication and characterization of Tungsten heavy alloys with high W content by powder metallurgy, Metall. Mater. Trans. A 53 (3) (2022) 1085–1098, https://doi.org/10.1007/s11661-021-06579-w

[72] M. Faleschini, H. Kreuzer, D. Kiener, R. Pippan, Fracture toughness investigations of tungsten alloys and SPD tungsten alloys, J. Nucl. Mater. 367–370 (2007) 800–805, https://doi.org/10.1016/j.jnucmat.2007.03.079

[73] M.A.M. Ghazali, M.A. Harimon, M.S. Mustapa, Mechanical behavior and microstructural analysis of molybdenum-TZM alloy subjected to different annealing temperature, JSE 1 (2019) 31–35, https://doi.org/10.30650/jse.v1i1.522

[74] B.V. Cockeram, The fracture toughness and toughening mechanisms of wrought low carbon arc cast, oxide dispersion strengthened, and molybdenum-0.5 pct titanium-0.1 pct zirconium molybdenum plate stock, Metall. Mater. Trans. A 36 (2005) 1777–1791, https://doi.org/10.1007/s11661-005-0042-2

[75] C. Chen, S.J. Pang, Y.Y. Cheng, T. Zhang, Microstructure and mechanical properties of $Al_{20-x}Cr_{20+0.5}xFe_{20}Co_{20}Ni_{20+0.5x}$ high entropy alloys, J. Alloy. Compd. 659 (2016) 279–287, https://doi.org/10.1016/j.jallcom.2015.10.258

[76] H. Zhang, Y.Z. He, Y. Pan, Enhanced hardness and fracture toughness of the laser-solidified FeCoNiCrCuTiMoAlSiB$_{0.5}$ high-entropy alloy by martensite strengthening, Scr. Mater 69 (4) (2013) 342–345, https://doi.org/10.1016/j.scriptamat.2013.05.020

[77] O.N. Senkov, G.B. Wilks, J.M. Scott, D.B. Miracle, Mechanical properties of $Nb_{25}Mo_{25}Ta_{25}W_{25}$ and $V_{20}Nb_{20}Mo_{20}Ta_{20}W_{20}$ refractory high entropy alloys, Intermetallics 19 (5) (2011) 698–706, https://doi.org/10.1016/j.intermet.2011.01.004

[78] Y. Zou, P. Okle, H. Yu, T. Sumigawa, T. Kitamura, S. Maiti, W. Steurer, R. Spolenak, Fracture properties of a refractory high-entropy alloy: in situ micro-cantilever and atom probe tomography studies, Scr. Mater. 128 (2017) 95–99, https://doi.org/10.1016/j.scriptamat.2016.09.036

[79] H. Dobbelstein, E.P. George, E.L. Gurevich, A. Kostka, A. Ostendorf, G. Laplanche, Laser metal deposition of refractory high-entropy alloys for high-throughput synthesis and structure-property characterization, Int. J. Extrem. Manuf. 3 (1) (2021) 015201, https://doi.org/10.1088/2631-7990/abcca8

[80] X.J. Fan, R.T. Qu, Z.F. Zhang, Remarkably high fracture toughness of HfNbTaTiZr refractory high-entropy alloy, J. Mater. Sci. Technol. 123 (2022) 70–77, https://doi.org/10.1016/j.jmst.2022.01.017

[81] R.S. Ganji, K.V. Rajulapati, K.B.S. Rao, Development of a multi-phase AlCuTaVW high-entropy alloy using powder metallurgy route and its mechanical properties, Trans. Indian Inst. Met. 73 (3) (2020) 613–618, https://doi.org/10.1007/s12666-020-01875-2